Kinetics or Transport – Whither Goes the Solid-State Battery Cathode?

Kaustubh G. Naik, Bairav S. Vishnugopi, and Partha P. Mukherjee[*]

School of Mechanical Engineering, Purdue University, West Lafayette, IN 47907, USA

[*]*Correspondence*: pmukherjee@purdue.edu

Abstract

Solid-state batteries (SSBs) hold the potential to enhance the energy density, power density and safety of conventional lithium-ion batteries. Realizing the theoretical promise of SSBs is predicated on the mechanistic design and comprehensive analysis of various solid-solid interfaces and microstructural features within the system. The spatial arrangement and composition of constituent phases (e.g., active material, solid electrolyte, binder) in the solid-state cathode dictate critical characteristics such as solid-solid point contacts or singularities within the microstructure, and percolation pathways for ionic/electronic transport. In this work, we present a comprehensive mesoscale discourse to interrogate the underlying microstructure-coupled kinetic-transport interplay and concomitant modes of resistances that evolve during electrochemical operation of SSBs. Based on a hierarchical physics-based analysis, the mechanistic implications of solid-solid point contact distribution and intrinsic transport pathways on the kinetic heterogeneity is established. Toward designing high-energy-density SSB systems, the fundamental correlation between active material loading, electrode thickness and electrochemical response has been delineated. We examine the paradigm of carbon-binder free cathodes and identify design criteria that can facilitate enhanced performance with such electrode configurations. A mechanistic design map highlighting the dichotomy in kinetic and ionic/electronic transport limitations that manifest at various SSB cathode microstructural regimes is established.

Keywords

solid-state batteries, cathode microstructure, kinetic-transport interactions, solid-solid point contacts, electrochemical performance.

1. Introduction

As conventional lithium-ion batteries (LIBs) approach their theoretical energy densities, there is a persistent need for the development of next-generation energy storage devices that can comply with demands of applications such as electric vehicles.[1, 2] In this regard, the utilization of lithium metal anodes, owing to their high specific capacity (3860 mAh g^{-1}) and low electrochemical potential (-3.04 V *vs* standard hydrogen electrode) promise to intrinsically boost the gravimetric and volumetric energy densities of LIBs.[3-6] In addition, replacing the organic liquid electrolyte with an inorganic solid electrolyte (SE)[7-9] can address the safety concerns of existing LIBs.[10] Due to the high cation transference number and inherent mechanical rigidity, SEs are also expected to bypass bulk polarization and enable compact deposition morphologies, thereby providing an exciting opportunity to achieve enhanced power density, safety and charging rates.[11-13]

Over the recent past, significant research efforts have been made towards the synthesis of SEs with enhanced ionic conductivities[14]. Notably, sulfide-based SEs have exhibited high ionic conductivities in the order of 10^{-3} S cm^{-1}, outperforming their liquid counterparts.[15, 16] Alongside the materials level, major research impetus has been laid on understanding the cell architectural aspects and various interfacial complexations that underlie the electrochemical performance of solid-state batteries (SSBs).[17-22] Promisingly, researchers have recently demonstrated an energy density of 900 W h L^{-1} over a life of 1000 cycles at 0.5 C-rate at the pouch cell level, incorporating solid argyrodite sulfide electrolytes.[23] Despite a few promising performance reports,[16, 23] several fundamental challenges pertaining to the morphological stability of the anode,[24-33] fabrication process of thin separators[34] and the design of composite cathode architectures[35, 36] still exist.

The electrochemical performance of SSB cells is largely correlated with the composition and spatial arrangement of the constituent phases in its composite cathode[37]. In addition to the active

material (AM) and SE, electrochemically inactive components such as the conductive additive and binder provide enhanced electron percolation pathways and mechanical integrity of the electrode respectively.[38, 39] However, carbon additives can potentially lead to degradation mechanisms at their interfaces with the SE, while the binder impedes ion and electron percolation pathways within the composite cathode microstructure.[19, 40-43] Furthermore, such secondary phases also block electrochemically active sites, thus contributing to both kinetic and transport resistances within the electrode. The inadequate solid-solid contact area between the AM and SE poses additional constraints on the electrochemical performance of SSBs.[44] Large volume fluctuations of the AM over cell operation can exacerbate this scenario by further depleting the electrical contact between the AM and SE particles.[43, 45-48] To enhance active contact area, strategies such as electrolyte-coated AM particles[49] and liquid-phase synthesized electrolytes[50] have been successfully employed to achieve improved cell performance.

Despite such recent advancements, performance of SSBs is rather limited at electrode compositions with a high AM loading (~ 80 wt. %). Nam *et al.*[51] and Zhang *et al.*[52] have revealed a decline in cell capacity and rate performance at such high cathode loadings. Contrary to liquid electrolyte systems, the energy density of SSBs is constrained by the presence of residual voids[53] and the requisite fraction (~30 wt. %) of SE particles to facilitate adequate ionic transport within the cathode.[54] To achieve high performance electrodes, it is critical to gain a fundamental understanding of the influence of design parameters such as the size and morphology of the AM and SE particles, secondary phase (i.e., conductive additive and binder) content and electrode thickness over a wide range of operating conditions. Prior studies in this regard have also highlighted the distinct benefits of improved ion and electron percolation pathways towards cell performance, via modulation of AM and SE particle sizes.[51, 54-56] Minnmann *et al*.[57] highlighted

that high AM loading can eliminate the necessity for carbon additives that are often used to improve the electronic conductivity of the cathode composite. Recently, Li *et al*.[58] has proposed the use of superior ionic/electronic mixing conductors as an alternative to carbon additives and electrolyte to maximize the energy density of SSBs.

While recent studies in literature have focused on understanding the ionic/electronic tortuosity and active area attributes of such solid-state cathodes,[41, 42, 54] a mechanistic demarcation of the transport and kinetic limitations during electrochemical operation of the SSB is still required. With percolation of transport pathways and solid-solid point contact within the cathode architecture being critical features that control cell performance, it is necessary to quantify their distinct implications at various electrode recipes and operating conditions. In the current work, we delineate the role of microstructural arrangement and composition of the composite cathode on the electrochemical response of the SSB. A hierarchical mesoscale modeling framework is developed, which quantifies effective electrode properties and systematically feeds the microstructural information to a macro-homogenous model that captures the electrochemical performance of the SSB. In order to enhance the energy density in SSB systems, a high AM loading in thicker electrode configurations, along with good AM utilization is required. The fundamental correlation between AM loading, thickness, and electrochemical utilization for such solid-state cathodes is analyzed based on the proposed mesoscale modeling strategy. We also quantify the distinct modes of resistances (i.e., kinetic and transport) within the cell at various cathode compositions and identify a non-monotonic trend in cell performance as the AM phase content is varied. Current focusing and the non-homogeneous reaction distribution within the electrode is quantified at different discharge rates and found to be one of the major aspects limiting the discharge capacity at higher cathode loadings. Furthermore, we investigate the paradigm of carbon-binder free

cathodes and demarcate design criteria that can potentially facilitate improved performance of such electrode configurations even at high AM loadings. Lastly, we summarize cathode microstructure-driven kinetic and transport-limited regimes and derive design guidelines for improved performance of SSBs. This work provides a fundamental insight into the mesoscale behavior of the solid-state cathode and enhancement in cell performance via electrode engineering.

2. Methodology

Figure 1(a) schematically illustrates a three-dimensional solid-state cathode microstructure consisting of active material (AM), carbon-binder (CBD), solid electrolyte (SE) and voids, along with its two-dimensional cross-section in Figure 1(b). $x = 0$ corresponds to the current collector side whereas $x = L_c$ corresponds to the separator side. In the current work, several realizations of the composite cathode microstructure have been stochastically generated by varying the fractions of constituent phases. The fraction of voids in the composite cathode is kept constant at 5% of the total volume. In contrast to liquid electrolyte systems, solid-solid particle contact and presence of voids leads to highly tortuous pathways for ions (see Figure 1(d)) which can have a significant impact on ionic conductivity. Effective electronic conductivity within the cathode is enhanced by the CBD phase as it improves electronic percolation pathways, in addition to offering a high intrinsic electronic conductivity. Figure 1(e) shows representative electron percolation pathways within the microstructural domain. Unlike liquid electrolytes that wet the surface of AM, the active surface area is limited by the particle-particle contact between AM and SE phases, which necessitates accurate estimation of active area for composite cathode microstructures (See Figure 1(c)). Stochastic generation of microstructures is performed using GeoDict[42, 59-61] where the voxel length, total number cells in x, y and z directions, volume fractions of the constituent phases and

diameter of AM and SE particles are provided as inputs. Effective electrode properties for each microstructure are estimated using direct numerical simulations (DNS).[60-62] It is noted that the control volume size (200μm×200μm×200μm) used in this study for effective electrode property estimation is sufficiently larger than the AM and SE particle sizes.[63] As a result, the effective electrode properties evaluated are truly determined by the cathode composition and have negligible errors arising due to the microstructural stochasticity.

Electrochemical reactions in composite cathode occur at the solid-solid interfacial contact between AM and SE phases. This active surface area is estimated using modified version of the Minkowski method[62, 63] as follows:

$$a_s = \frac{4\pi I_{AM-SE}}{M_x M_y M_z \Delta} f \tag{1}$$

Here, I_{AM-SE} represent the number of cell faces having AM and SE cell on either side, M_x, M_y, and M_z represent the total number of cells in x, y, and z directions, respectively, and Δ represents the voxel length. The digitized sphere of radius $r = N\Delta$, represented by the surface faces, I_N, approaches the ideal sphere as the number of surface faces is sufficiently high. The parameter, $f = \frac{N^2}{I_N}$ is obtained based on the convergence of the digitized sphere's surface area towards the ideal sphere's surface area ($4\pi r^2$). It is noted that this method is valid for any geometry, thus allowing us to compute the interfacial area between AM and SE phases.

Tortuosity computation involves solving the Laplace equation for electrical potential which is given as follows:

$$\nabla^2 \phi = 0 \tag{2}$$

For the estimation of x-direction tortuosity, τ_x, boundary conditions corresponding to $\phi(x = 0) = \phi_{left}$ and $\phi(x = L_c) = \phi_{right}$ are applied on two extreme faces of the composite cathode. On the remaining faces ($y = 0, z = 0, y = L_y, z = L_z$), we set $\frac{\partial \phi}{\partial n} = 0$. Solution obtained from Eq. 2 can then be used to estimate flux by integrating the potential gradient over one of the extreme faces ($x = 0\ or\ x = L_c$). The corresponding tortuosity can then be evaluated from the equation given below:

$$j_x = -D\frac{\varepsilon_{SE}}{\tau_x}\left[\frac{\phi_{right} - \phi_{left}}{L_c}\right] = -D\frac{\varepsilon_{SE}}{\tau_x}\left(\frac{1}{L_c}\right) \tag{3}$$

where, ε_{SE} is the SE volume fraction, D is the intrinsic transport coefficient and j_x is the flux in x-direction. Tortuosity in y and z directions can be calculated by suitably rearranging the boundary conditions mentioned above. It is noted that the intrinsic transport coefficient, D, is set to unity for SE phase and zero for AM, CBD and voids for the estimation of tortuosity in SE phase. Based on the tortuosity values estimated from Eq. 3, the effective ionic conductivity in the x, y and z directions are computed as follows:

$$\kappa_i^{eff} = \kappa\frac{\varepsilon_{SE}}{\tau_{SE,i=x,y,z}} \tag{4}$$

where, κ is the intrinsic ionic conductivity and $\tau_{SE,i}$ is the ionic tortuosity within the SE. The effective ionic conductivity of SE is then estimated by using the arithmetic mean of tortuosity obtained for the x, y and z directions.

Effective electronic conductivity in the AM-CBD phase can be estimated using a similar procedure that has been outlined for ionic conductivity of the composite cathode. Relevant properties for the constituent phases of composite cathode are summarized in Table S1 of Supporting Information.

Butler-Volmer kinetics is used to describe the electrochemical reaction occurring at the active AM-SE contact and is expressed as follows:

$$i = i_0 \left[\exp\left(\frac{F}{2RT}\eta\right) - \exp\left(\frac{-F}{2RT}\eta\right) \right] \tag{5}$$

where, i_0 is exchange current density, F is Faraday constant, R is universal gas constant, T is temperature and η is overpotential. The exchange current density, i_0, is given by the following expression:

$$i_0 = Fk(c_e)^{0.5}\left(c_{s,max} - c_s\right)^{0.5}(c_s)^{0.5} \tag{6}$$

Here, k is the rate of reaction, c_e is the lithium-ion concentration in SE, c_s is the lithium concentration in AM particles and $c_{s,max}$ is the maximum lithium concentration that can be inserted in AM particles.

Spherical geometry has been considered for the AM particles, within which the lithium transport has been solved using Ficksian diffusion in radial coordinates as given below:

$$\frac{\partial c_s}{\partial t} = \frac{1}{r^2}\frac{\partial}{\partial r}\left(D_s r^2 \frac{\partial c_s}{\partial r}\right) \tag{7}$$

where, c_s is lithium concentration, D_s is AM phase diffusivity, r is radial coordinate and t is time. Electric potential (ϕ_s) in AM domain can be solved using Ohm's law as follows:

$$\nabla.(\sigma^{eff}\nabla\phi_s) - j = 0 \tag{8}$$

Here, σ^{eff} is effective electronic conductivity and j is volumetric current density. Moreover, the electric potential (ϕ_{SE}) for ionic transport in the SE domain can be estimated using charge conservation as shown below:

$$\nabla \cdot (\kappa^{eff} \nabla \phi_{SE}) + j = 0 \tag{9}$$

where, κ^{eff} is the effective ionic conductivity in the SE phase. Volumetric current density can be expressed in terms of active area (a_s) and current density (i) as follows:

$$j = a_s i \tag{10}$$

In this modeling framework, the concentration of lithium ions in the SE phase of the composite cathode is considered to be constant due to the high cationic transference number that results in negligible concentration gradients in the SE. All the parameters used in the modeling framework are listed in Table S2 of Supporting Information.

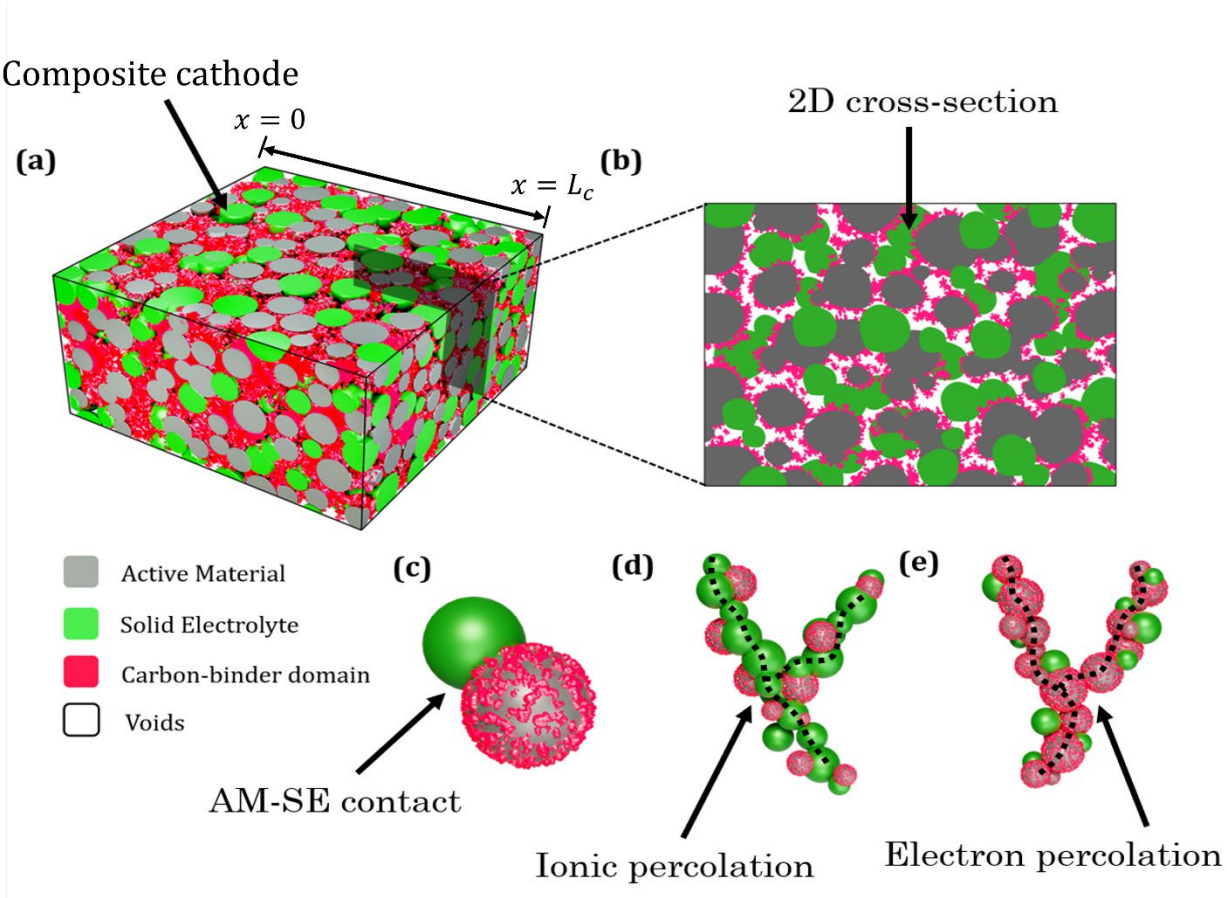

Figure 1. (a) Representative illustration of a composite solid-state cathode microstructure consisting of AM, SE, CBD, and voids. (b) Cross-sectional view of the electrode, depicting the spatial distribution of ionic and electronic-conductive phases. Microstructural arrangement and

composition dictate key electrode performance attributes including (c) active contact area, (d) ionic and (e) electronic percolation pathways. Dependent on the applied current rates and electrode composition, these pore-scale features strongly influence the evolution of kinetic and transport resistances over cell operation.

3. Results and Discussion

Figure 2(a-c) presents the variation in effective electrode properties, namely tortuosity for ion transport, active area, and effective electronic conductivity, as a function of electrode composition. As shown in Figure 2(a), in general, an increase in AM loading and secondary phase (CBD) content results in larger tortuosities for ionic transport within the SE particle network. While increasing the AM content from 40 to 60 wt. % results in only a moderate tortuosity rise, further increase in AM loading (from 60 to 80 wt. %) is found to substantially reduce the ion percolation pathways. For instance, for a CBD fraction of 4 wt. %, tortuosity increases from 1.3 at 40 wt. % AM to 1.5 at 60 wt.% AM. However, with an increase in AM loading to 80 wt.%, tortuosity increases up to a magnitude of 4. In addition, as depicted in Figure 2(a), the effect of CBD content on ionic transport is more severe in the regime of high AM loading (> 60wt. %). Effective ionic conductivities of the SE phase are calculated using Eq. 4, which has been described in the Methodology section. Analogous to the trends in tortuosity, an increase in CBD content reduces the effective conductivity, by preventing the connectivity of ion percolation pathways (see Figure S1 of Supporting Information). Towards the regime of 80 wt.% AM, a substantial reduction in effective conductivities, when compared to the intrinsic property (0.039 S/m) is observed. In contrast to the trends in tortuosity, active area (see Figure 2(b)) is dissimilarly influenced by increase in AM and CBD content. At lower fractions of CBD (0-2 wt. %), an increase in AM loading from 40 to 80 wt. % leads to roughly a four-fold enhancement in the active area. However, at larger fractions of CBD (4-6 wt. %) with CBD phase covering the interfacial contact sites, active

area remains almost unaffected with variation in AM loading. With increasing AM loading at higher CBD fractions (4-6 wt. %), active area slightly increases, reaches maximum and then decreases with further increase in AM loading. Here, in addition to the CBD phase covering the AM surface, a very low SE fraction unable to cover the available AM surface area has a negative impact on the active area. Overall, an increase in the CBD content, required to enhance the effective electronic conductivity of the composite electrode results in a significant reduction of the active interfacial area due to AM surface area blockage by CBD phase, insufficient SE phase to cover the AM surface, AM-AM contact further preventing the AM-SE contact. More detailed analysis of the trend observed for the active area is discussed in section S6 of the Supporting Information. As illustrated in Figure 2(c), an increase in CBD content from 0 to 6 wt. % leads to significant enhancement in electronic conductivity at all regimes of AM loading. While a higher AM loading results in improved electron percolation pathways owing to the lower tortuosity in the AM phase, this improvement is substantially amplified with increase in CBD content. Overall, we infer that CBD content of the electrode presents a major tradeoff between effective ionic conductivity and active area versus effective electronic conductivity, especially in the design of cathode architectures with high AM loading. Figure 2(d) and Figure 2(e) presents 3D and its cross-sectional representations of the distribution of active area sites for kinetically-limiting (40 wt. % AM, 6 wt. % CBD, 54 wt. % SE) and kinetically-non-limiting (80 wt.% AM, 3 wt.% CBD, 17 wt. % SE) scenarios. The kinetically-limiting scenario arises due to insufficient availability of active area, which leads to increased overpotentials at AM-SE interface. As shown in Figure 2(d), the presence of such point contacts or singularities within the microstructure are critical descriptors that dictate the kinetic limitations in SSB cathodes. A 2D representation of the constituent phases in composite cathode, along with the corresponding interfacial active area map is presented in

Figure S7 of the Supporting Information. As seen from Figure 2(b), low AM content and/or high CBD content results in reduced active area that enhances the focusing of reaction current at the available interfacial contact sites. Limited connectivity amongst these contact sites (see Figure 2(d)) further increases the overpotential and exacerbates the kinetic limitation within the cathode microstructure. On the other hand, high AM and low CBD composition regimes result in improved active area regimes as represented in Figure 2(e). Additionally, the uniformity and connectivity in the contact sites promotes a homogenous distribution of electrochemical reaction, resulting in reduced overpotentials and kinetic resistance. Further comparison and quantification of the internal kinetic and transport resistances for these scenarios has been presented in Figure 3.

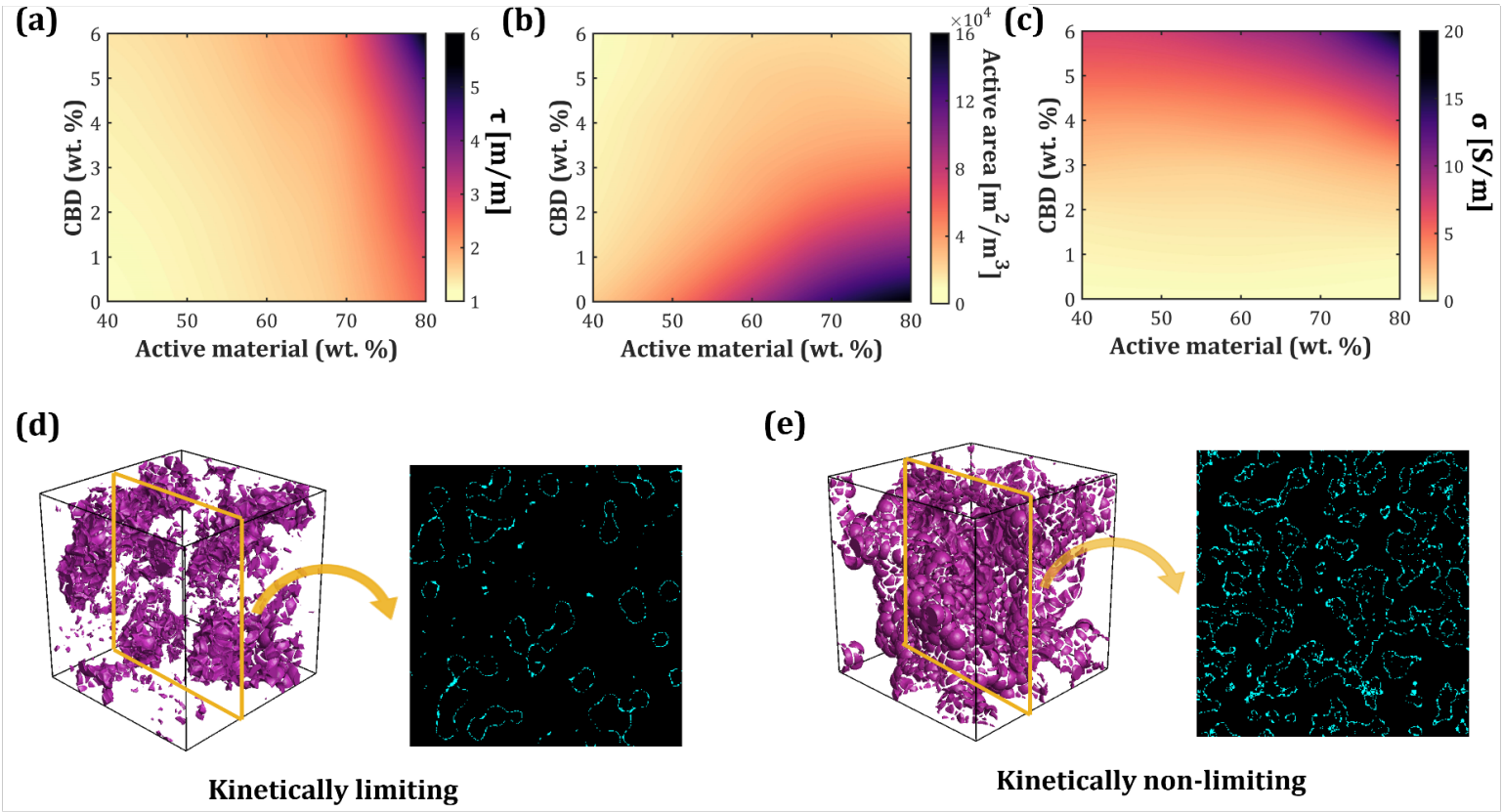

Figure 2. Estimation of effective electrode properties: (a) tortuosity for ionic transport (b) electrochemically active area and (c) electronic conductivity as a function of the AM and CBD

content (each in wt. %). Three-dimensional and two-dimensional representation of interfacial active area distribution (interface between AM and SE) for (d) kinetically-limiting (40 wt. % AM, 6 wt. % CBD, 54 wt. % SE) and (e) kinetically-non-limiting (80 wt.% AM, 3 wt.% CBD, 17 wt. % SE) scenarios.

Based on the computed effective electrode properties, we subsequently analyze the electrochemical performance of the SSB. Internal kinetic and ionic/electronic transport resistance modes have been quantified to understand the implication of different electrode parameters. An increase in AM loading results in a non-monotonic variation in cell discharge capacity for each CBD fraction (see section S2 of Supporting Information). Discharge capacities steadily increase, reach a maximum value, and then decrease with further increase in the AM content. A quantitative comparison of the modeling results with a recent experimental report [57] has been provided in section S5 of the Supporting Information, showing very good agreement. At lower fractions of the CBD phase, the maximum discharge capacity is achieved at a higher AM loading (Figure S2 of Supporting Information). In other words, without undergoing major limitations on electronic percolation, reduced fractions of the CBD phase can enhance the performance at higher AM loading owing to the improved ionic percolation pathways (due to lower CBD content) and increased active area (due to higher AM content). The corresponding electrochemical performance signatures for 40-60-80 wt. % AM and 3-6 wt. % CBD content has been presented in Figure 3(a). As discussed in Figure 2, increasing the AM content from 40 wt. % to 60 wt. % results in minimal rise in tortuosity of SE phase, implying that ionic transport resistance is not significantly affected. At the same time, the active area is remarkably improved (see Figure 2(b)) resulting in significant drop in kinetic resistance, which improves the electrochemical performance at 60 wt. % AM as shown in Figure 3(a). Reduction in cell capacities as we move from 60 to 80 wt.% AM loading is a strong function of the associated CBD content in the electrode. While an increase in CBD content

from 3 to 6 wt. % results in negligible capacity decay at 40 and 60 wt. % AM, a severe reduction in discharge capacity from 115 to 50 mAh/g is observed at 80 wt. % AM. The beneficial effect on the active area with an increase in AM loading is clearly negated by the reduction in ion percolation pathways. Although CBD content improves the overall electronic conductivity, larger fractions (especially in the regime of 3-6 wt. %) have a negative implication on both the active area and effective ionic conductivity. The three internal resistive modes within the solid-state cathode, namely, kinetic, electronic and ionic transport resistances, and the corresponding overpotentials can be mathematically expressed as follows:

Kinetic resistance:

$$R_{kin} = \frac{\eta_{kin}}{I_{app}} \tag{11}$$

$$\eta_{kin} = \frac{1}{L_c}\int_{L_c} \eta \, dx \tag{12}$$

Electronic resistance:

$$R_{elec} = \frac{\eta_{elec}}{I_{app}} \tag{13}$$

$$\eta_{elec} = \Delta\phi_{AM-CBD}|_{0-L_c} \tag{14}$$

Ionic resistance:

$$R_{ionic} = \frac{\eta_{ionic}}{I_{app}} \tag{15}$$

$$\eta_{ionic} = \Delta\phi_{SE}|_{0-L_c} \tag{16}$$

Here, η is the overpotential used in Eq. 5, L_c is cathode thickness, $\Delta\phi_{AM-CBD}$ is potential drop in AM-CBD phase and $\Delta\phi_{SE}$ is potential drop in SE phase and I_{app} is the applied current density. Figure 3(b) quantifies these resistive modes for two specific cases in the electrode design spectrum: 40 wt. % AM, 3 wt. % CBD, 57 wt. % SE and 80 wt. % AM, 6 wt. % CBD, 14 wt. % SE. In both these cases, the contribution from ohmic resistance in the AM-CBD phase is found to be negligibly small owing to the high intrinsic value of electronic conductivity for the CBD phase. Interestingly, the relative severity of ionic transport resistance (related to the ohmic drop in SE phase) and kinetic resistance is different at scenarios of low and high AM loading. While the unavailability of active interfacial area makes kinetic overpotential as the chief resistance mode at a low AM loading, ohmic drop in the SE domain is found to govern the performance of cathodes with high AM loading. In addition, an increase in AM loading results in a steep rise in ionic transport resistance over cell operation (lower panel of Figure S3(a) in Supporting Information). This effect on transport resistance is largely correlated to the localization of reactions that take place in such cathode architectures. This phenomenon will be explained in later stages of the results section.

In Figure 3(c), electrochemical performance for 40, 60 and 80 wt. % AM are presented for two different applied currents, i.e., 4 mA/cm^2 and 7 mA/cm^2. Trends in discharge capacities are similar to that observed in Figure 3(a), where capacities increase from 40 wt. % AM to 60 wt. % AM and exhibit a sharp decay at 80 wt. % AM. Capacity decay at 80 wt. % AM can be attributed to the ionic transport limitation due to increased tortuosity in the SE phase. For both 40 and 60 wt. % AM compositions, the effect of applied current on the final discharge capacity is observed to be negligibly small. However, the effect of applied current is more severe at higher AM loadings, as shown in Figure 3 (c) for 80 wt. % AM. Higher applied current densities necessitate faster transport rates within the cathode microstructure, which at very high AM compositions (≈ 80 wt. % AM)

becomes rate-limiting and results in increased ionic transport resistance and capacity decay. Figure 3(d) compares distinct resistive signatures within cathode microstructure for 40 wt. % AM, 4 mA/cm^2 and 80 wt. % AM, 7 mA/cm^2. At regimes of high AM content and with increase in applied current densities, ionic transport resistance is inferred to be the primary performance-limiting mechanism. At 40 wt. % and 60 wt. % AM loading, lower tortuosity allows efficient ionic transport for both 4 mA/cm^2 and 7 mA/cm^2 current densities. At low AM loading (40 wt. % AM), insufficient active area results in higher kinetic resistance limiting the cell performance. In both the cases shown in Figure 3(d), electron transport resistance in the AM-CBD domain is negligibly small, owing to the high intrinsic electronic conductivity of the CBD phase. Kinetic and ionic transport resistances for the cases considered in Figure 3 are tabulated in Table S3 and Table S4 of the Supporting Information (electron transport resistance is very low for all the cases considered in Figure 3).

Figure 3(e-g) represent how θ (particle level state-of-charge) evolves with discharge capacity across the cathode thickness. Figure 3(h) represents the electric potential (for ionic transport) in the SE domain over the non-dimensional cathode thickness $\left({}^{l}/_{L_{cathode}}\right)$. As depicted in Figure 3(e), for a low AM loading and current density of 4 mA/cm^2, at a particular instance, the state of charge remains almost the same over the entire cathode thickness. Also, for the corresponding plot in Figure 3(h), minimal potential drop in the SE domain is observed. Lower drop in potential across the SE phase implies reduced ionic resistances that promote a homogenous state of charge distribution across the electrode. It is noted that high θ levels (or complete AM utilization) are reached over the entire cathode thickness by the end of discharge.

In Figure 3(f), the state of charge (θ) evolution has been presented for the same applied current density, while changing the AM content to 80 wt. %. In contrast to the previous case, θ levels vary

significantly across the cathode thickness. While maximum AM utilization is observed near the separator due to localized electrochemical reactions, the utilization is substantially lowered at regions near the current collector. Due to the relatively high potential drop in SE as depicted by the corresponding plot in Figure 3(h), ion transport resistance increases resulting in the localization of reactions near the separator. For high AM loading (80 wt. %) and an applied current density of 7 mA/cm^2 (Figure 3(g)), major sections of the cathode near the current collector remain unutilized (very low θ levels) even towards the end of discharge. This is largely correlated to the higher ohmic resistance in the SE domain, as corroborated by the electric potential distribution in Figure 3(h). At faster discharge conditions, thicker cathodes with high AM loading are observed to deliver severely limited discharge capacities. However, to achieve higher energy densities in solid-state cathodes, design of thicker cathodes is preferred. Hence, addressing the ion transport limitation in such cathode configurations is essential. In Figure S4 of Supporting Information, the differences in θ values at two ends of the cathode are summarized for different electrode compositions and current densities. Based on the analysis, it is reiterated that the high AM content (80 wt. %) along with an increased current density can lead to an unutilized cathode regime near the current collector. The intermediate range of AM content (60-70 wt. %) is identified to be the most appropriate choice at a wider range of applied current densities for the considered cathode thickness (70μm). In the subsequent section, we will investigate the potential effect of cathode thickness on AM utilization, internal resistance, and cell performance.

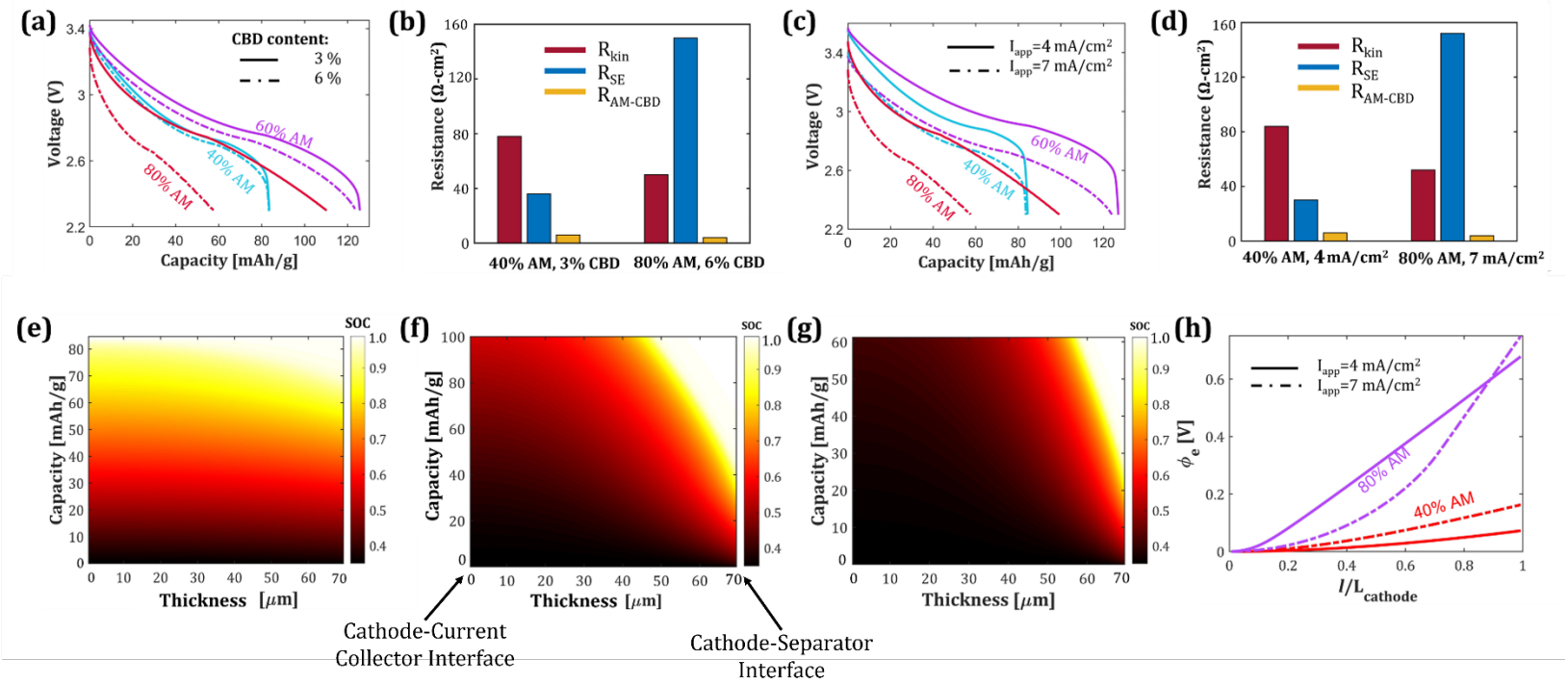

Figure 3. (a) Electrochemical performance signatures at varying electrode compositions for applied current density of 7 mA/cm^2. (b) Comparison of underlying resistive modes for electrode compositions of 40 wt.% AM, 3 wt. % CBD, 57 wt. % SE and 80 wt. % AM, 6 wt. % CBD, 14 wt. % SE. (c) Effect of applied current density on cell performance at 40, 60 and 80 wt.% AM loading having 6 wt.% CBD. (d) Comparison of underlying resistive modes for 40 wt.% AM, 4 mA/cm^2 and 80 wt.% AM, 7 mA/cm^2. Evolution of particle level state-of-charge (θ) with the discharge capacity along cathode thickness for (e) 40 wt. % AM, 6 wt. % CBD, 54 wt. % SE and applied current density of 4 mA/cm^2 (f) 80 wt. % AM, 6 wt. % CBD, 14 wt. % SE and applied current density of 4 mA/cm^2 (g) 80 wt. % AM, 6 wt. % CBD, 14 wt. % SE and applied current density of 7 mA/cm^2. (h) Variation of electric potential along the non-dimensional cathode thickness $\left(l/L_{cathode}\right)$ for varying electrode composition. Cathode thickness is 70μm for all the cases presented here.

Figure 4 presents the implications of cathode thickness on cell performance at a current density of 7 mA/cm^2. Figure 4(b) presents the schematic illustration of thin and thick cathodes with a representative ionic percolation pathway. With an increase in thickness, we identify additional resistances that contribute to a reduction in performance, as shown in Figure 4(a). The correlation between cathode thickness and performance is explained using the AM utilization maps that are

depicted in Figure 4(d) and Figure 4(e). For a cathode thickness of 40μm, complete AM utilization is achieved at the end of discharge as depicted in Figure 4(d). On the other hand, for thicker cathode of 100μm, regions near the current collector remain relatively unutilized due to current focusing near the separator. In Figure 4(f), comparison of resistance modes, i.e., kinetic, ionic, and electronic transport resistances are shown for the two extreme cases considered (40μm and 100μm). Resistance values show a clear shift from kinetically-limiting regime to transport-limited regime as we move toward thicker cathodes. Resistance to ionic transport within thicker cathodes is substantially higher as compared to thinner cathodes. It is noted that the contribution from ohmic resistance in the AM-CBD phase is negligibly small owing to high intrinsic electronic conductivity of the CBD phase. Kinetic resistance for both the thicknesses are almost identical as the same composition leads to similar availability of the active area – this leaves ionic transport resistance as the differential factor that needs to be considered when moving from thinner to thicker electrodes. In Figure 4(c), the electric potential in SE phase is computed as a function of non-dimensional cathode thickness for the three cases (40μm, 70μm and 100μm) considered in Figure 4(a). As described above, potential drop for the 100μm cathode is the largest followed by 70μm and 40μm thicknesses, which can be directly correlated to the severity in ionic transport resistance. Also, the slope of electric potential profile for thin cathode (40μm) is almost same over the entire electrode thickness (except near the current collector). But as the electrode thickness is increased, the slope of electric potential profile is smaller near the current collector side, and it increases towards the separator side. As ionic current is determined by the gradient of the electric potential, the ionic current is almost uniform in the thin cathodes. But for the thicker cathodes, ionic current is majorly localized near the separator indicating under-utilization of cathode near the current collector. Also, it is interesting to note that the electric potential lines in Figure 4(c) intersect almost

at the same point, towards the separator side of which, the gradient of electric potential for thicker cathodes is larger.

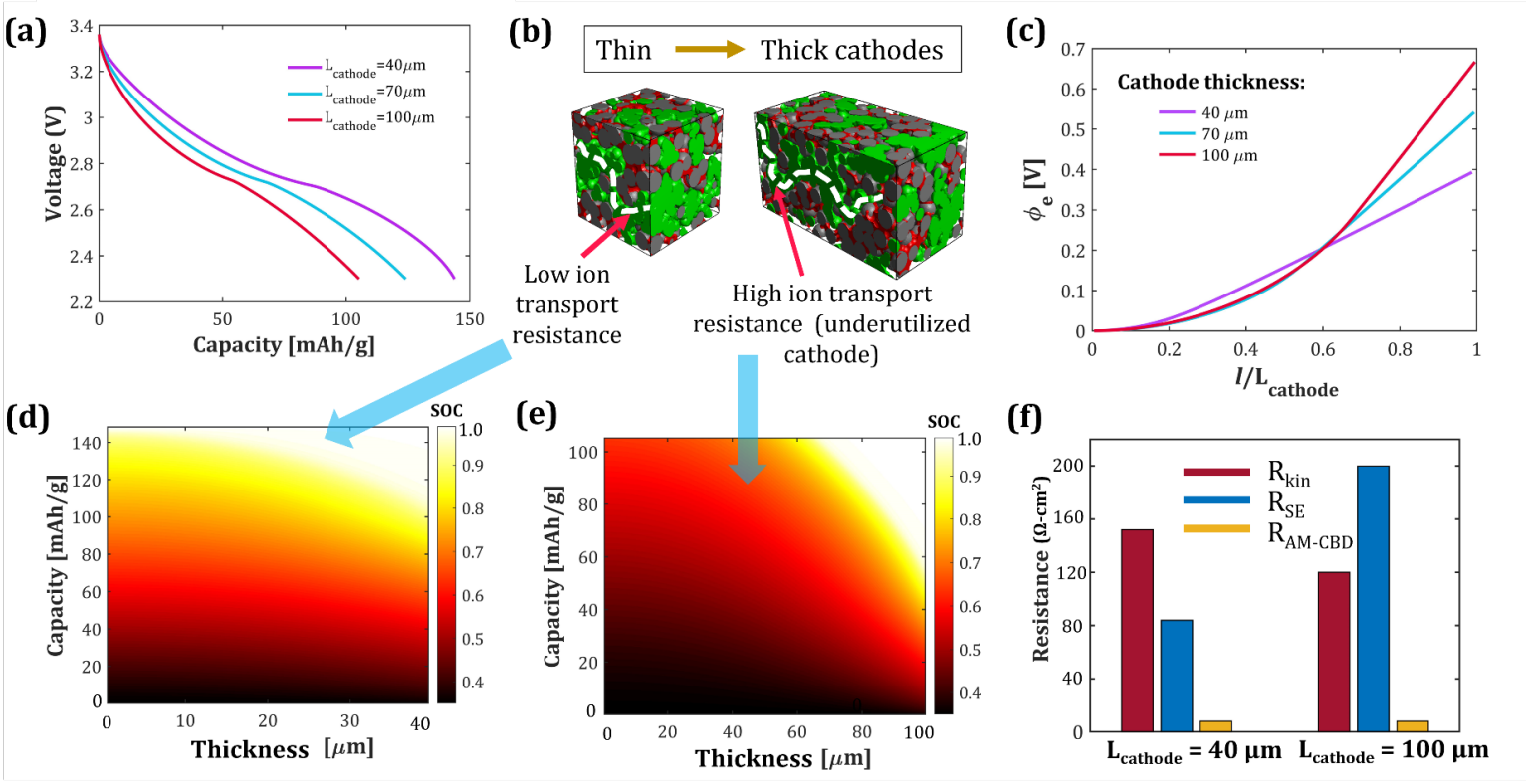

Figure 4. (a) Electrochemical performance signatures for different cathode thicknesses of 40μm, 70μm and 100μm with the composition of 70 wt. % AM, 6 wt. % CBD, 24 wt. % SE and applied current density of 7 mA/cm^2. (b) Schematic representation of ionic percolation pathways (dominant resistive mode) in thin and thick cathodes (c) Electric potential in the SE phase as a function of non-dimensional cathode thickness for the three cases considered in (a). (d) Evolution of particle level state-of-charge (θ) for the lower bound of the cathode thickness considered, that is, 40μm. (e) Evolution of particle level state-of-charge (θ) for the upper bound of the cathode thickness considered, i.e., 100μm. (f) Comparison of the underlying resistance modes for the two extremes of cathode thicknesses considered, that is, 40μm and 100μm.

Based on the mesoscale modeling framework, Figures 5(a) and 5(b) demarcate the electrode recipe and operating conditions that have been observed to result in enhanced performance at the cell level. In Figure 5(a), a design phase map in terms of dimensionless discharge capacity, C/C^0, is

constructed for varying electrode compositions, while fixing a constant thickness (70μm) and current density (7 mA/cm^2). Here C is the actual capacity achieved and C^0 is the theoretical capacity of the AM. As shown in Figure 5(a), the *preferred regime* is demarcated at 65-75 wt. % AM and 1-4 wt. % CBD. Due to the insufficient active area available in low AM content compositions (40-50 wt. % AM) and increased tortuosity (decreased ionic conductivity) in very high AM content compositions (80 wt. % AM), reduced discharge capacities are obtained in both cases. Thus, an initial increase in the AM loading (40 to 70 wt. % AM) increases the energy density, but further increase in AM loading reduces the energy density due to the underlying transport limitations of high AM loading cathodes. Also, increasing the CBD content, especially at a higher AM loading (≥ 70 wt. % AM), shows a steep decline in the discharge capacity, having negative implications on the energy density. In the design map shown in Figure 5(b), dimensionless discharge capacities are represented as a function of applied current density and electrode thickness, while maintaining the constant composition (70 wt. % AM, 6 wt. % CBD, 24 wt. % SE). For thinner cathodes (40-60μm), high discharge capacities are obtained for a wide range of applied current densities due to reduced transport resistance and enhanced utilization of the AM. With an increase in current density, lower discharge capacities are observed for a cathode thickness > 60μm. As shown in Figure 5(b), as the cathode thickness increases above 60μm, achieving higher capacities mandates the application of lower current densities. While Figures 5(a) and 5(b) classify favorable electrode recipes, moving towards high-energy-density cathodes that can sustain faster current rates would require targeted improvement in ion percolation pathways, while not compromising on the active area and electronic conductivity.

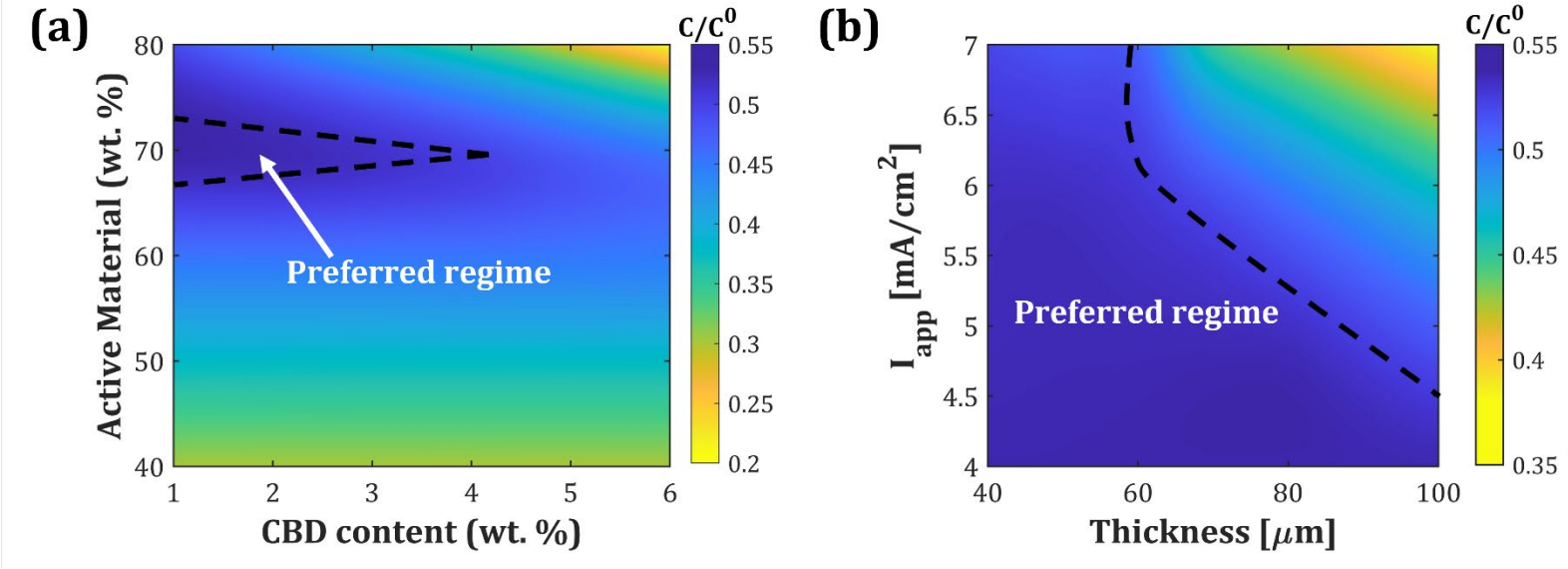

Figure 5. Phase maps of dimensionless discharge capacity, C/C^0, (a) for varying electrode compositions (AM + CBD content) at a current density of 7 mA/cm^2 and electrode thickness of 70μm. (b) for different electrode thicknesses and applied current densities with electrode composition fixed at 70 wt. % AM, 6 wt. % CBD, 24 wt. % SE.

In this section, we explore the potential of cathode designs with minimal incorporation of secondary phases (conductive additive and binder) and assess the underlying performance attributes. As discussed previously, while the incorporation of such additional phases aid in improving mechanical integrity and overall electronic conductivity, they reduce the available active area (Figure 2(b)) and result in tortuous ion transport pathways (Figure 2(a)). Also, in a previous study[64], it has been observed that the incorporation of carbon additives in the composite cathode can lead to decomposition of the SE, resulting in interfacial resistance build up and capacity fade. Theoretically, constructing composite cathodes without such additional phases should reduce internal kinetic and ion transport resistances and contribute to a direct increase in energy density. Figure 6(a) presents the cell capacity trends for varying AM fractions, with no secondary phases incorporated (the constituent phases in the cathode are only AM and SE). As shown in Figure 6(a), the discharge capacity obtained for such compositions are significantly lower

than the previous cases (Figure 3-5). However, the trend in discharge capacities with variation in AM content remains quite similar. Relatively higher discharge capacities are obtained for composition with 60-70 wt. % AM, whereas discharge capacities for cathode compositions with low (40 wt. % AM) and high (80 wt. % AM) AM loadings are significantly reduced (20 mAh/g). In contrast to the previously studied cases (Figure 3-5), ohmic drop within the AM-CBD phase is found to be the chief mode of internal resistance for both 40 wt. % and 80 wt. % AM as shown in Figure 6(b). This is due to the inherently low electronic conductivity of the AM (see Table S1 of Supporting Information) and the reduction in electronic percolation pathways due to absence of the conductive additives. Additionally, as shown in Figure 6(b), the ionic transport resistance is larger for 80 wt. % AM than 40 wt. % AM, whereas the kinetic resistances are approximately the same for both the compositions. While these secondary phase-free cathode compositions are limited by electron transport, they negate critical challenges with respect to ionic tortuosity and active area (Figure 2). To understand the theoretical electronic conductivity limit of the AM that is required to overcome electron percolation limitations, we conduct a performance sensitivity analysis, as illustrated in Figure 6(c). While maintaining other electrode properties (i.e., tortuosity, ionic conductivity and active area) constant, only the intrinsic electronic conductivity of the AM is increased for each composition and the resulting influence on cell performance is studied. It is noted that the first data point for each plot corresponds to the actual electronic conductivity of the AM (as tabulated in Table S1 of Supporting Information) and the corresponding discharge capacity. As observed in Figure 6(c), with an increase in electronic conductivity from its actual value to 0.01 S/m, an approximately 300% increase in discharge capacity is obtained for 40 wt. % AM. The corresponding capacity increase is 150% and 650% for 60 wt. % AM and 80 wt. % AM, respectively. Beyond a certain limit of electronic conductivity (approximately 0.01 S/m),

improvement in discharge capacity saturates, implying that electronic conductivity is no longer a limiting factor. It is inferred that this limit signifies a fundamental transition from an electron transport-limited to an ion transport-limited regime for cell performance. Interestingly, the highest saturation capacity is obtained for 80 wt. % AM loading. Thus, with further improvements in intrinsic electronic conductivity of the cathode, such design configurations with minimal incorporation of secondary phases promise to mitigate challenges pertaining to ion transport and availability of active interfacial sites for achieving homogeneous reaction distributions. In addition to minimizing the use of secondary phases, minimizing the void space within composite cathode is also important to mitigate the kinetic and transport limitations. In this regard, approaches such as bimodal or trimodal particle size distribution can potentially improve the performance of SSBs.[41] Lastly, we note that while the focus of this work is to understand the underlying role of reaction kinetics and ionic/electronic transport based on the geometric arrangement of the constituent phases, the potential effect of intrinsic material interfaces (e.g., role of carbon additive on interphase formation/SE decomposition) has not been considered and will be included in a future study.

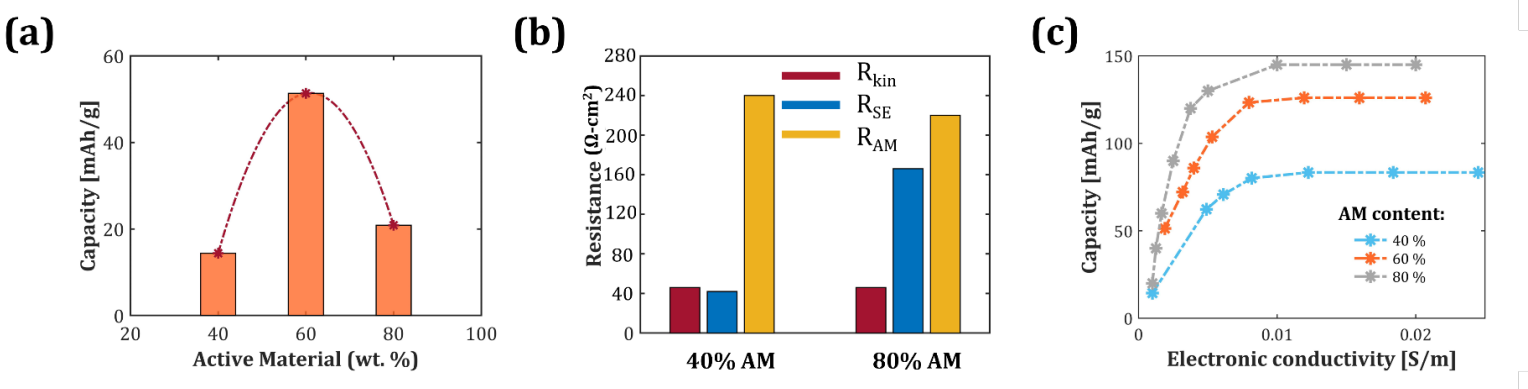

Figure 6. (a) Discharge capacity as a function of AM content for cathode compositions without the incorporation of secondary phases (conductive additive + binder). (b) Comparison of the key resistance modes over cell operation for 40 wt. % and 80 wt. % AM. (c) Performance sensitivity test depicting the variation in discharge capacity with increase in intrinsic electronic conductivity of the AM.

As discussed in the earlier sections, the interplay between kinetic, ion transport and electron transport resistances plays a pivotal role in determining cell performance. Cathode composition regimes in Figure 7 are demarcated based on whether the microstructure is: (I) kinetically-limited, (II) ion transport-limited, or (III) electron transport-limited. Firstly, low AM content (≈ 40 wt. %) results in insufficient active area leading to a kinetically-limiting scenario. Also, at low AM content, there is a higher possibility for the presence of isolated AM-CBD clusters (see Figure 7). Such isolated AM-CBD clusters do not contribute to the electronic percolation pathways and thus remain unutilized during cell operation. At compositions with a higher CBD content, kinetic limitations arise as the CBD phase covers a significant amount of AM surface reducing the solid-solid contact points between AM and SE. Secondly, ion transport limitation occurs at high AM content due to increased tortuosity in the SE phase (See Figure 7). At a higher CBD content, ion transport limitation becomes more severe and thus occur at a relatively low AM content (≈ 67 wt. %) as shown in Figure 7. Lower fraction of the SE results in isolated SE clusters that further exacerbate the ionic transport resistance. Similar to isolated AM-CBD clusters in the kinetically-limiting case, these isolated SE clusters remain largely inactive. As discussed in the earlier section (see Figure 4), ionic transport resistance is the chief resistive mode in thicker cathodes resulting in unutilized AM and localized reactions due to longer ionic percolation pathways. Lastly, electron transport limitation is observed at very low fractions of the CBD phase as shown in Figure 7. In this regime, insufficient distribution of the CBD phase leads to poor connectivity between AM particles and increases the electron transport resistance. Electron transport limitations shift towards lower CBD content (see Figure 7) at high AM loadings due to improved connectivity between AM particles. It is noted that some cathode composition regimes can also have two dominant resistive

modes as shown in Figure 7. With high AM and high CBD content, the electrode is both kinetically and ion transport-limited; at low AM and very low CBD content, kinetic and electron transport limitations are the most dominant, whereas at high AM and high CBD content, both electron and ion transport limitations simultaneously occur. Cathode compositions marked in green denote minimal contribution from all three modes of internal resistances resulting in improved performance of the SSB.

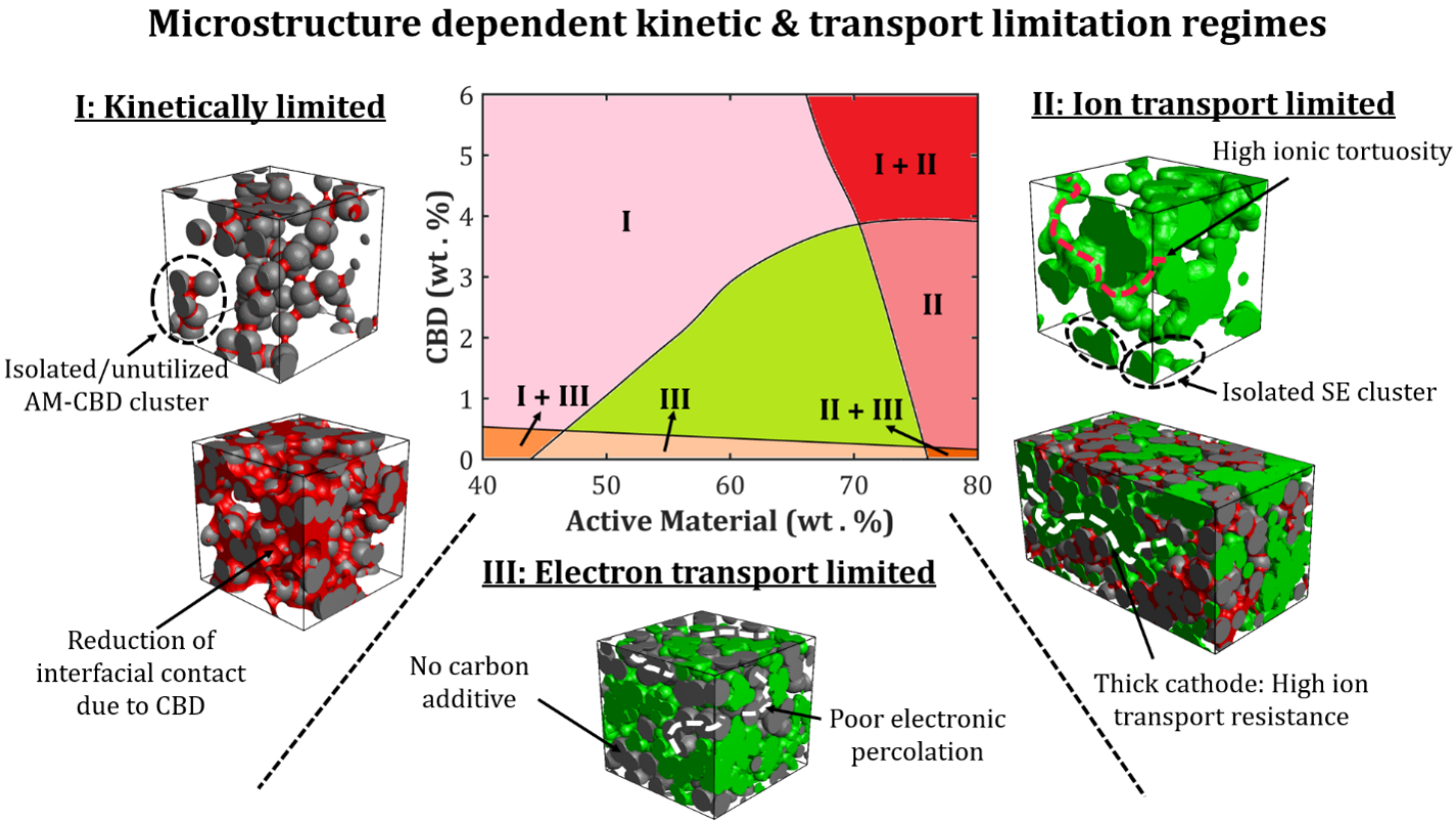

Figure 7. Cathode composition regimes, based on three limiting mechanisms: (I) Kinetic limitation (II) Ion transport limitation and (III) Electron transport limitation, along with schematic illustrations depicting the major factors that dictate the corresponding internal resistive modes.

4. Conclusion

Overall, this work provides a fundamental insight into the microstructure-coupled kinetic-transport interactions underlying the electrochemical response of SSB cathodes. The dichotomy in kinetic and ionic/electronic transport limitations that arise at various electrode recipes and operating conditions is comprehensively analyzed. The mechanistic coupling between the distribution of solid-solid point contacts, percolation pathways and evolution of internal resistance through cell operation is described. We highlight the critical role played by the distribution of point contacts or singularities within the microstructure in regulating the kinetic limitations. The amount and spatial arrangement of secondary phases is an important design factor for cathodes especially at high AM loading. Electrodes with high energy density (via increased thickness/AM loading) and/or faster operating rates results in a significant non-homogeneity in reaction kinetics, current focusing and limited electrochemical utilization of the electrode, primarily attributed to inefficient ionic transport pathways. Towards achieving high-energy-density SSB systems, eliminating the use of secondary phases can serve as a potential strategy. In this regard, kinetic and transport signatures of cathode designs with zero secondary phase content is explored and the correlation between intrinsic electronic conductivity of AM and cell performance is delineated. We construct a comprehensive design map, highlighting the microstructure-driven kinetic-transport interplay and future considerations to achieve optimal performance of SSB cathodes.

Acknowledgements

Financial support in part from the National Science Foundation (award no.: 2041499) and the Alfred P. Sloan Foundation through a Scialog – Advanced Energy Storage award is gratefully acknowledged.

Conflict of Interest

There are no conflicts to declare.

Supporting Information

(Table S1) Relevant properties for constituent phases considered in composite cathodes; (Table S2) parameters used in the model; (Table S3-S4) ionic and kinetic resistances for varying cathode compositions; (Section S1, Figure S1) quantification of ionic conductivity in solid electrolyte phase; (Section S2, Figure S2) composition dependent electrochemical performance analysis; (Section S3, Figure S3) evolution of internal resistance over cell operation; (Section S4, Figure S4) quantifying cathode utilization using state of charge; (Section S5, Table S5, Figure S5) model verification; (Section S6, Figure S6) composition dependent active area analysis; (Section S7, Figure S7) solid-solid interfaces between AM-SE particles

References:

1. Choi, J. W.; Aurbach, D., Promise and Reality of Post-Lithium-Ion Batteries with High Energy Densities. *Nature Reviews Materials* **2016,** *1* (4), 1-16.
2. Nitta, N.; Wu, F.; Lee, J. T.; Yushin, G., Li-Ion Battery Materials: Present and Future. *Materials today* **2015,** *18* (5), 252-264.
3. Lin, D.; Liu, Y.; Cui, Y., Reviving the Lithium Metal Anode for High-Energy Batteries. *Nature nanotechnology* **2017,** *12* (3), 194.
4. Guo, Y.; Li, H.; Zhai, T., Reviving Lithium-Metal Anodes for Next-Generation High-Energy Batteries. *Advanced materials* **2017,** *29* (29), 1700007.
5. Cheng, X.-B.; Zhang, R.; Zhao, C.-Z.; Zhang, Q., Toward Safe Lithium Metal Anode in Rechargeable Batteries: A Review. *Chemical reviews* **2017,** *117* (15), 10403-10473.
6. Xu, W.; Wang, J.; Ding, F.; Chen, X.; Nasybulin, E.; Zhang, Y.; Zhang, J.-G., Lithium Metal Anodes for Rechargeable Batteries. *Energy & Environmental Science* **2014,** *7* (2), 513-537.
7. Hayashi, A.; Hama, S.; Morimoto, H.; Tatsumisago, M.; Minami, T., Preparation of Li2s–P2s5 Amorphous Solid Electrolytes by Mechanical Milling. *Journal of the American Ceramic Society* **2001,** *84* (2), 477-79.
8. Kanno, R.; Murayama, M., Lithium Ionic Conductor Thio-Lisicon: The Li2 S Ges2 P 2 S 5 System. *Journal of the electrochemical society* **2001,** *148* (7), A742.

9. Mizuno, F.; Hayashi, A.; Tadanaga, K.; Tatsumisago, M., New, Highly Ion-Conductive Crystals Precipitated from Li2s–P2s5 Glasses. *Advanced Materials* **2005,** *17* (7), 918-921.
10. Liu, J.; Bao, Z.; Cui, Y.; Dufek, E. J.; Goodenough, J. B.; Khalifah, P.; Li, Q.; Liaw, B. Y.; Liu, P.; Manthiram, A., Pathways for Practical High-Energy Long-Cycling Lithium Metal Batteries. *Nature Energy* **2019,** *4* (3), 180-186.
11. Hatzell, K. B.; Chen, X. C.; Cobb, C. L.; Dasgupta, N. P.; Dixit, M. B.; Marbella, L. E.; McDowell, M. T.; Mukherjee, P. P.; Verma, A.; Viswanathan, V., Challenges in Lithium Metal Anodes for Solid-State Batteries. *ACS Energy Letters* **2020,** *5* (3), 922-934.
12. Krauskopf, T.; Richter, F. H.; Zeier, W. G.; Janek, J. r., Physicochemical Concepts of the Lithium Metal Anode in Solid-State Batteries. *Chemical Reviews* **2020,** *120* (15), 7745-7794.
13. Vishnugopi, B. S.; Kazyak, E.; Lewis, J. A.; Nanda, J.; McDowell, M. T.; Dasgupta, N. P.; Mukherjee, P. P., Challenges and Opportunities for Fast Charging of Solid-State Lithium Metal Batteries. *ACS Energy Letters* **2021,** *6*, 3734-3749.
14. Wu, J.-F.; Pang, W. K.; Peterson, V. K.; Wei, L.; Guo, X., Garnet-Type Fast Li-Ion Conductors with High Ionic Conductivities for All-Solid-State Batteries. *ACS applied materials & interfaces* **2017,** *9* (14), 12461-12468.
15. Hayashi, A.; Noi, K.; Tanibata, N.; Nagao, M.; Tatsumisago, M., High Sodium Ion Conductivity of Glass–Ceramic Electrolytes with Cubic Na3ps4. *Journal of Power Sources* **2014,** *258*, 420-423.
16. Kato, Y.; Hori, S.; Saito, T.; Suzuki, K.; Hirayama, M.; Mitsui, A.; Yonemura, M.; Iba, H.; Kanno, R., High-Power All-Solid-State Batteries Using Sulfide Superionic Conductors. *Nature Energy* **2016,** *1* (4), 1-7.
17. Janek, J.; Zeier, W. G., A Solid Future for Battery Development. *Nature Energy* **2016,** *1* (9), 1-4.
18. Banerjee, A.; Wang, X.; Fang, C.; Wu, E. A.; Meng, Y. S., Interfaces and Interphases in All-Solid-State Batteries with Inorganic Solid Electrolytes. *Chemical reviews* **2020,** *120* (14), 6878-6933.
19. Culver, S. P.; Koerver, R.; Zeier, W. G.; Janek, J., On the Functionality of Coatings for Cathode Active Materials in Thiophosphate-Based All-Solid-State Batteries. *Advanced Energy Materials* **2019,** *9* (24), 1900626.
20. Kim, A.-Y.; Strauss, F.; Bartsch, T.; Teo, J. H.; Hatsukade, T.; Mazilkin, A.; Janek, J. r.; Hartmann, P.; Brezesinski, T., Stabilizing Effect of a Hybrid Surface Coating on a Ni-Rich Ncm Cathode Material in All-Solid-State Batteries. *Chemistry of Materials* **2019,** *31* (23), 9664-9672.
21. Bucci, G.; Swamy, T.; Chiang, Y.-M.; Carter, W. C., Modeling of Internal Mechanical Failure of All-Solid-State Batteries During Electrochemical Cycling, and Implications for Battery Design. *Journal of Materials Chemistry A* **2017,** *5* (36), 19422-19430.
22. Zahiri, B.; Patra, A.; Kiggins, C.; Yong, A. X. B.; Ertekin, E.; Cook, J. B.; Braun, P. V., Revealing the Role of the Cathode–Electrolyte Interface on Solid-State Batteries. *Nature Materials* **2021,** *20* (10), 1392-1400.
23. Lee, Y.-G.; Fujiki, S.; Jung, C.; Suzuki, N.; Yashiro, N.; Omoda, R.; Ko, D.-S.; Shiratsuchi, T.; Sugimoto, T.; Ryu, S., High-Energy Long-Cycling All-Solid-State Lithium Metal Batteries Enabled by Silver–Carbon Composite Anodes. *Nature Energy* **2020,** *5* (4), 299-308.
24. Cheng, E. J.; Sharafi, A.; Sakamoto, J., Intergranular Li Metal Propagation through Polycrystalline Li6. 25al0. 25la3zr2o12 Ceramic Electrolyte. *Electrochimica Acta* **2017,** *223*, 85-91.
25. Krauskopf, T.; Hartmann, H.; Zeier, W. G.; Janek, J. r., Toward a Fundamental Understanding of the Lithium Metal Anode in Solid-State Batteries—an Electrochemo-Mechanical Study on the Garnet-Type Solid Electrolyte Li6. 25al0. 25la3zr2o12. *ACS applied materials & interfaces* **2019,** *11* (15), 14463-14477.
26. Kasemchainan, J.; Zekoll, S.; Spencer Jolly, D.; Ning, Z.; Hartley, G. O.; Marrow, J.; Bruce, P. G., Critical Stripping Current Leads to Dendrite Formation on Plating in Lithium Anode Solid Electrolyte Cells. *Nat. Mater* **2019,** *18* (10), 1105-1111.

27. Lewis, J. A.; Cortes, F. J. Q.; Liu, Y.; Miers, J. C.; Verma, A.; Vishnugopi, B. S.; Tippens, J.; Prakash, D.; Marchese, T. S.; Han, S. Y., Linking Void and Interphase Evolution to Electrochemistry in Solid-State Batteries Using Operando X-Ray Tomography. *Nature Materials* **2021,** *20* (4), 503-510.
28. Mistry, A.; Mukherjee, P. P., Molar Volume Mismatch: A Malefactor for Irregular Metallic Electrodeposition with Solid Electrolytes. *Journal of the Electrochemical Society* **2020,** *167* (8), 082510.
29. Verma, A.; Kawakami, H.; Wada, H.; Hirowatari, A.; Ikeda, N.; Mizuno, Y.; Kotaka, T.; Aotani, K.; Tabuchi, Y.; Mukherjee, P. P., Microstructure and Pressure-Driven Electrodeposition Stability in Solid-State Batteries. *Cell Reports Physical Science* **2021,** *2* (1), 100301.
30. Lewis, J. A.; Cortes, F. J. Q.; Boebinger, M. G.; Tippens, J.; Marchese, T. S.; Kondekar, N.; Liu, X.; Chi, M.; McDowell, M. T., Interphase Morphology between a Solid-State Electrolyte and Lithium Controls Cell Failure. *ACS Energy Letters* **2019,** *4* (2), 591-599.
31. Shen, F.; Dixit, M. B.; Xiao, X.; Hatzell, K. B., Effect of Pore Connectivity on Li Dendrite Propagation within Llzo Electrolytes Observed with Synchrotron X-Ray Tomography. *ACS Energy Letters* **2018,** *3* (4), 1056-1061.
32. Vishnugopi, B. S.; Dixit, M. B.; Hao, F.; Shyam, B.; Cook, J. B.; Hatzell, K. B.; Mukherjee, P. P., Mesoscale Interrogation Reveals Mechanistic Origins of Lithium Filaments Along Grain Boundaries in Inorganic Solid Electrolytes. *Advanced Energy Materials* **2022,** *12* (3), 2102825.
33. Kazyak, E.; Garcia-Mendez, R.; LePage, W. S.; Sharafi, A.; Davis, A. L.; Sanchez, A. J.; Chen, K.-H.; Haslam, C.; Sakamoto, J.; Dasgupta, N. P., Li Penetration in Ceramic Solid Electrolytes: Operando Microscopy Analysis of Morphology, Propagation, and Reversibility. *Matter* **2020,** *2* (4), 1025-1048.
34. Zhang, Z.; Shao, Y.; Lotsch, B.; Hu, Y.-S.; Li, H.; Janek, J.; Nazar, L. F.; Nan, C.-W.; Maier, J.; Armand, M., New Horizons for Inorganic Solid State Ion Conductors. *Energy & Environmental Science* **2018,** *11* (8), 1945-1976.
35. Lewis, J. A.; Tippens, J.; Cortes, F. J. Q.; McDowell, M. T., Chemo-Mechanical Challenges in Solid-State Batteries. *Trends in Chemistry* **2019,** *1* (9), 845-857.
36. Dixit, M. B.; Parejiya, A.; Muralidharan, N.; Essehli, R.; Amin, R.; Belharouak, I., Understanding Implications of Cathode Architecture on Energy Density of Solid-State Batteries. *Energy Storage Materials* **2021,** *40*, 239-249.
37. Dixit, M.; Parejiya, A.; Essehli, R.; Muralidharan, N.; Haq, S. U.; Amin, R.; Belharouak, I., Solidpac Is an Interactive Battery-on-Demand Energy Density Estimator for Solid-State Batteries. *Cell Reports Physical Science* **2022**, 100756.
38. Oh, D. Y.; Nam, Y. J.; Park, K. H.; Jung, S. H.; Kim, K. T.; Ha, A. R.; Jung, Y. S., Slurry-Fabricable Li+-Conductive Polymeric Binders for Practical All-Solid-State Lithium-Ion Batteries Enabled by Solvate Ionic Liquids. *Advanced Energy Materials* **2019,** *9* (16), 1802927.
39. Riphaus, N.; Strobl, P.; Stiaszny, B.; Zinkevich, T.; Yavuz, M.; Schnell, J.; Indris, S.; Gasteiger, H. A.; Sedlmaier, S. J., Slurry-Based Processing of Solid Electrolytes: A Comparative Binder Study. *Journal of The Electrochemical Society* **2018,** *165* (16), A3993.
40. Li, X.; Ren, Z.; Norouzi Banis, M.; Deng, S.; Zhao, Y.; Sun, Q.; Wang, C.; Yang, X.; Li, W.; Liang, J., Unravelling the Chemistry and Microstructure Evolution of a Cathodic Interface in Sulfide-Based All-Solid-State Li-Ion Batteries. *ACS Energy Letters* **2019,** *4* (10), 2480-2488.
41. Bielefeld, A.; Weber, D. A.; Janek, J. r., Modeling Effective Ionic Conductivity and Binder Influence in Composite Cathodes for All-Solid-State Batteries. *ACS applied materials & interfaces* **2020,** *12* (11), 12821-12833.
42. Bielefeld, A.; Weber, D. A.; Janek, J. r., Microstructural Modeling of Composite Cathodes for All-Solid-State Batteries. *The journal of physical chemistry C* **2018,** *123* (3), 1626-1634.
43. Hao, F.; Mukherjee, P. P., Mesoscale Analysis of the Electrolyte-Electrode Interface in All-Solid-State Li-Ion Batteries. *Journal of The Electrochemical Society* **2018,** *165* (9), A1857.
44. Wan, H.; Mwizerwa, J. P.; Qi, X.; Xu, X.; Li, H.; Zhang, Q.; Cai, L.; Hu, Y.-S.; Yao, X., Nanoscaled Na3ps4 Solid Electrolyte for All-Solid-State Fes2/Na Batteries with Ultrahigh Initial

Coulombic Efficiency of 95% and Excellent Cyclic Performances. *ACS applied materials & interfaces* **2018,** *10* (15), 12300-12304.
45. Koerver, R.; Zhang, W.; de Biasi, L.; Schweidler, S.; Kondrakov, A. O.; Kolling, S.; Brezesinski, T.; Hartmann, P.; Zeier, W. G.; Janek, J., Chemo-Mechanical Expansion of Lithium Electrode Materials–on the Route to Mechanically Optimized All-Solid-State Batteries. *Energy & Environmental Science* **2018,** *11* (8), 2142-2158.
46. Koerver, R.; Aygün, I.; Leichtweiß, T.; Dietrich, C.; Zhang, W.; Binder, J. O.; Hartmann, P.; Zeier, W. G.; Janek, J. r., Capacity Fade in Solid-State Batteries: Interphase Formation and Chemomechanical Processes in Nickel-Rich Layered Oxide Cathodes and Lithium Thiophosphate Solid Electrolytes. *Chemistry of Materials* **2017,** *29* (13), 5574-5582.
47. Zhang, W.; Schröder, D.; Arlt, T.; Manke, I.; Koerver, R.; Pinedo, R.; Weber, D. A.; Sann, J.; Zeier, W. G.; Janek, J., (Electro) Chemical Expansion During Cycling: Monitoring the Pressure Changes in Operating Solid-State Lithium Batteries. *Journal of Materials Chemistry A* **2017,** *5* (20), 9929-9936.
48. Barai, P.; Rojas, T.; Narayanan, B.; Ngo, A. T.; Curtiss, L. A.; Srinivasan, V., Investigation of Delamination-Induced Performance Decay at the Cathode/Llzo Interface. *Chemistry of Materials* **2021,** *33* (14), 5527-5541.
49. Banerjee, A.; Park, K. H.; Heo, J. W.; Nam, Y. J.; Moon, C. K.; Oh, S. M.; Hong, S. T.; Jung, Y. S., Na3sbs4: A Solution Processable Sodium Superionic Conductor for All-Solid-State Sodium-Ion Batteries. *Angewandte Chemie* **2016,** *128* (33), 9786-9790.
50. Yao, X.; Liu, D.; Wang, C.; Long, P.; Peng, G.; Hu, Y.-S.; Li, H.; Chen, L.; Xu, X., High-Energy All-Solid-State Lithium Batteries with Ultralong Cycle Life. *Nano letters* **2016,** *16* (11), 7148-7154.
51. Nam, Y. J.; Oh, D. Y.; Jung, S. H.; Jung, Y. S., Toward Practical All-Solid-State Lithium-Ion Batteries with High Energy Density and Safety: Comparative Study for Electrodes Fabricated by Dry-and Slurry-Mixing Processes. *Journal of Power Sources* **2018,** *375*, 93-101.
52. Zhang, W.; Weber, D. A.; Weigand, H.; Arlt, T.; Manke, I.; Schröder, D.; Koerver, R.; Leichtweiss, T.; Hartmann, P.; Zeier, W. G., Interfacial Processes and Influence of Composite Cathode Microstructure Controlling the Performance of All-Solid-State Lithium Batteries. *Acs Applied Materials & Interfaces* **2017,** *9* (21), 17835-17845.
53. Hlushkou, D.; Reising, A. E.; Kaiser, N.; Spannenberger, S.; Schlabach, S.; Kato, Y.; Roling, B.; Tallarek, U., The Influence of Void Space on Ion Transport in a Composite Cathode for All-Solid-State Batteries. *Journal of Power Sources* **2018,** *396*, 363-370.
54. Shi, T.; Tu, Q.; Tian, Y.; Xiao, Y.; Miara, L. J.; Kononova, O.; Ceder, G., High Active Material Loading in All-Solid-State Battery Electrode Via Particle Size Optimization. *Advanced Energy Materials* **2020,** *10* (1), 1902881.
55. Strauss, F.; Bartsch, T.; de Biasi, L.; Kim, A.-Y.; Janek, J. r.; Hartmann, P.; Brezesinski, T., Impact of Cathode Material Particle Size on the Capacity of Bulk-Type All-Solid-State Batteries. *ACS Energy Letters* **2018,** *3* (4), 992-996.
56. Davis, A. L.; Goel, V.; Liao, D. W.; Main, M. N.; Kazyak, E.; Lee, J.; Thornton, K.; Dasgupta, N. P., Rate Limitations in Composite Solid-State Battery Electrodes: Revealing Heterogeneity with Operando Microscopy. *ACS Energy Letters* **2021,** *6* (8), 2993-3003.
57. Minnmann, P.; Quillman, L.; Burkhardt, S.; Richter, F. H.; Janek, J., Editors' Choice—Quantifying the Impact of Charge Transport Bottlenecks in Composite Cathodes of All-Solid-State Batteries. *Journal of The Electrochemical Society* **2021,** *168* (4), 040537.
58. Li, M.; Liu, T.; Shi, Z.; Xue, W.; Hu, Y. s.; Li, H.; Huang, X.; Li, J.; Suo, L.; Chen, L., Dense All-Electrochem-Active Electrodes for All-Solid-State Lithium Batteries. *Advanced Materials* **2021**, 2008723.
59. Graingeo Handbook, in Geodict 2022 User Guide from Math2market Gmbh, Germany. doi.org/10.30423/userguide.geodict2022.
60. Vishnugopi, B. S.; Verma, A.; Mukherjee, P. P., Fast Charging of Lithium-Ion Batteries Via Electrode Engineering. *Journal of The Electrochemical Society* **2020,** *167* (9), 090508.

61. Chen, C.-F.; Verma, A.; Mukherjee, P. P., Probing the Role of Electrode Microstructure in the Lithium-Ion Battery Thermal Behavior. *Journal of The Electrochemical Society* **2017,** *164* (11), E3146.
62. Mistry, A. N.; Smith, K.; Mukherjee, P. P., Secondary-Phase Stochastics in Lithium-Ion Battery Electrodes. *ACS applied materials & interfaces* **2018,** *10* (7), 6317-6326.
63. Parmananda, M.; Norris, C.; Roberts, S. A.; Mukherjee, P. P., Probing the Role of Multi-Scale Heterogeneity in Graphite Electrodes for Extreme Fast Charging. *ACS Applied Materials & Interfaces* **2022**.
64. Zhang, W.; Leichtweiß, T.; Culver, S. P.; Koerver, R.; Das, D.; Weber, D. A.; Zeier, W. G.; Janek, J. r., The Detrimental Effects of Carbon Additives in Li10gep2s12-Based Solid-State Batteries. *ACS applied materials & interfaces* **2017,** *9* (41), 35888-35896.

Table of Contents Graphic

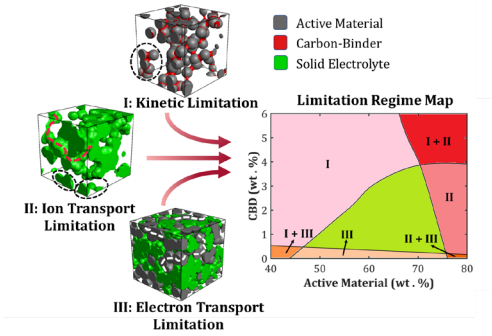

Supporting Information

Kinetics or Transport – Whither Goes the Solid-State Battery Cathode?

Kaustubh G. Naik, Bairav S. Vishnugopi, and Partha P. Mukherjee[*]

School of Mechanical Engineering, Purdue University, West Lafayette, IN 47907, USA

[*]*Correspondence*: pmukherjee@purdue.edu

Table S1. Relevant properties for constituent phases considered in composite cathodes[1-3]

Constituent Phase Material	**Density (g/cm^3)**	**Intrinsic electronic conductivity (S/m)**	**Intrinsic ionic conductivity (S/m)**	**Particle diameter (µm)**
NMC622 (AM)	4.7	1.06×10^{-3}	N/A	10
PVDF/C (Secondary Phase)	1.78	760	N/A	N/A
β-Li_3PS_4 (SE)	1.87	N/A	0.039	3

Table S2. Parameters used in the model

Parameters		**Values**	**Units**
k	Reaction rate constant for NMC622	2.57×10^{-11}	$m^{2.5}\ mol^{-0.5}\ s^{-1}$
R	Gas constant	8.314	$J\ mol^{-1}\ K^{-1}$
F	Faraday constant	96,487	$C\ mol^{-1}$
N_a	Avogadro constant	6.022×10^{23}	mol^{-1}
k_b	Boltzmann constant	1.38×10^{-23}	$m^2\ kg\ s^{-2}\ K^{-1}$
T	Operating temperature	298.15	K
L_s	Separator thickness	40	μm

a_0	Cross-sectional area	0.02	m^2
$c_{s_{max}}$	Maximum lithium concentration	52500	mol m^{-3}
x_{in}	Initial state of charge	0.35	
D_s	Active material diffusivity	3×10^{-14}	m^2 s^{-1}
Open Circuit Potential (U_0) of NMC622[4]	$U_0 = 13.4905 - 10.96038\,\theta + 8.203617\,(\theta)^{1.358699} - 3.10758 * 10^{-6} * \exp(127.1216\,\theta - 114.2593) - 7.033556\,(\theta)^{-0.03362749}$ [V]		

Table S3. Ionic and kinetic resistances for varying cathode compositions at cathode thickness of 70μm and applied current density of 7 mA/cm^2.

Sr no.	wt. % AM	wt. % SE	wt. % CBD	R_{kin}(Ω-cm^2)	R_{SE}(Ω-cm^2)
1.	40	57	3	79	37
2.	40	54	6	87	45
3.	60	37	3	26	53
4.	60	34	6	38	62
5.	80	17	3	16	94
6.	80	14	6	50	149

Table S4. Ionic and kinetic resistances for varying cathode compositions at cathode thickness of 70μm and applied current density of 4 mA/cm^2.

Sr no.	wt. % AM	wt. % SE	wt. % CBD	R_{kin}(Ω-cm^2)	R_{SE}(Ω-cm^2)
1.	40	54	6	82	30
2.	60	34	6	29	41
3.	80	14	6	36	71

S1. Quantification of ionic conductivity in solid electrolyte phase

As mentioned in the manuscript, tortuosity in the solid electrolyte (SE) phase is calculated by solving the Laplace equation for electric potential. Ionic conductivity values are obtained by using Eq. 3 of manuscript which is written below:

$$\kappa_i^{eff} = \kappa \frac{\varepsilon_{SE}}{\tau_{SE,i=x,y,z}} \quad (3)$$

Ionic conductivity values are plotted for specific values of active material (AM) and carbon-binder (CBD) wt. % as shown in Fig. S1. Since the ionic conductivity is the strong function of the tortuosity, ionic conductivities show decreasing trend as AM and CBD content is increased. Lower ionic conductivities at higher CBD content and AM loading results in the increase in ionic transport resistance as shown in Fig. 3 of manuscript.

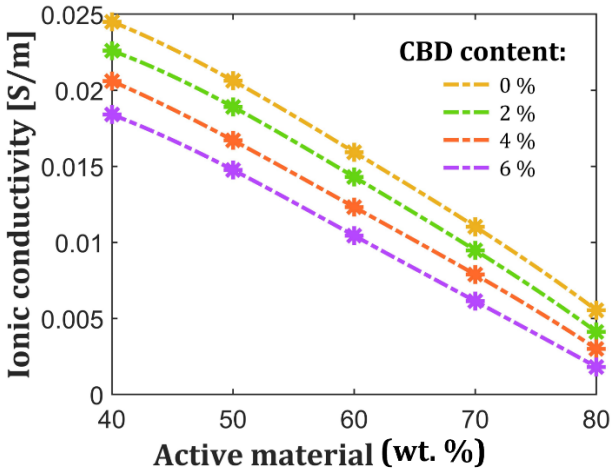

Figure S1: Effective ionic conductivity in SE phase as a function of AM and CBD content (each in wt. %).

S2. Composition dependent electrochemical performance analysis

In Fig. S2, discharge capacity is presented as a function of AM wt. % for different CBD contents. As we increase the AM content, discharge capacity rises, reaches maximum value, and then decreases at higher AM content. Discharge capacities for lower CBD content are higher owing to the improved ionic percolation and active area while not sacrificing much on electronic percolation. At lower AM content, electrochemical performance is kinetically limited, whereas, at very high AM content, it is transport limited resulting in the non-monotonic trend in the discharge capacities.

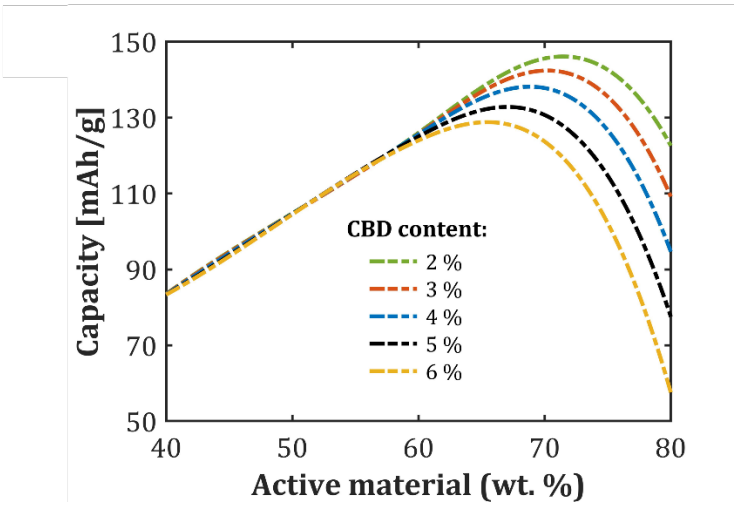

Figure S2. Discharge capacity as a function of AM and CBD content for applied current of 7 mA/cm^2, cathode thickness of 70µm and particle sizes provided in Table S1.

S3: Evolution of internal resistance over cell operation

In this section, we study the evolution of internal resistances, namely, kinetic, ionic, and electronic during the discharge operation. These resistances are plotted as a function of discharge capacity for 40 wt. % AM, 3 wt. % CBD and 80 wt. % AM, 6 wt. % CBD in Fig. S3(a) and for 40 wt. % AM, 4 mA/cm^2 and 80 wt. % AM, 7 mA/cm^2 in Fig. S3(b). For all the cases shown in Fig. S3, resistance due to electronic percolation is negligible owing to the high intrinsic electronic conductivity of CBD phase. At low AM content compositions, resistance due to kinetic overpotential is the largest due to the low active area available for electrochemical reactions. Whereas, at high AM content compositions, due to sufficient availability of active area resulting in low overpotential, kinetic resistance is observed to be reduced. Ionic transport resistance (resistance due to potential drop in SE phase) is much lower at low AM compositions due to lower tortuous pathways in SE phase. At higher AM and CBD compositions, due to increase in tortuosity,

ionic transport resistance is significantly higher. Also, it is noted that, a steep rise in ionic transport resistance is observed over the cell operation for compositions with higher AM loading.

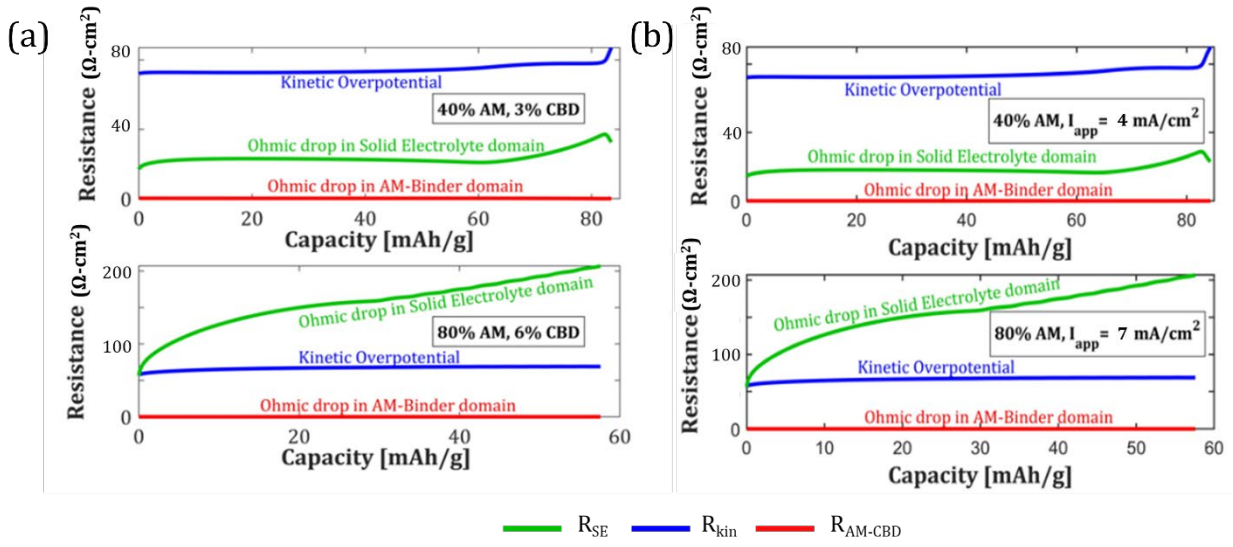

Figure S3. (a) Evolution of underlying resistive modes over cell operation at electrode compositions of 40 wt.% AM, 3 wt. % CBD, 57 wt. % SE and 80 wt.% AM, 6 wt. % CBD, 14 wt. % SE at applied current density of 7 mA/cm^2 and electrode thickness of 70µm. (b) Evolution of underlying resistive modes over cell operation for 40 wt.% AM, 4 mA/cm^2 and 80 wt.% AM, 7 mA/cm^2 at 6 wt. % CBD and cathode thickness 70µm.

S4. Quantifying cathode utilization using state of charge

Fig. S4 represents the differences in state of charge (ΔSOC) at the two ends of the cathode for varying composition and applied current densities. ΔSOC can be considered as a measure of cathode utilization, meaning, greater the ΔSOC value, poor is the cathode utilization. On the other hand, lesser ΔSOC value corresponds to efficient utilization of cathode. Utilization of cathode is a strong function of ionic transport resistance. More resistance to ions in SE phase leads to poor utilization of cathode. As seen in Fig. S4, low AM content and low applied current density yields

better cathode utilization owing to efficient ion transport through SE phase. High AM content leas to highly tortuous pathways in SE phase resulting in poor ion transport and hence, poor utilization. Also, during high applied current density operation, ions do not get sufficient time to percolate from one end of the cathode to the other, resulting in under-utilization. Part of the cathode near current collector remains unutilized in such cases leading to localization of reaction. For example, at 80 wt. % AM and 7 mA/cm^2 of applied current density, ΔSOC is more than 0.4. This means at the end of discharge, state of charge of AM near separator is 1, while the state of charge of AM near current collector is reached only 0.6.

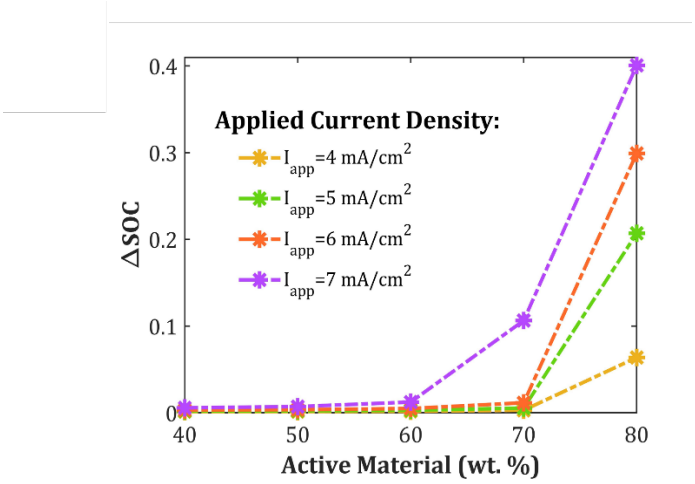

Figure S4. Difference in state of charge ΔSOC at the two ends of the cathode as a function of composition and applied current density. Here, the electrode thickness is 70μm and the CBD fraction is kept constant at 3 wt. %

S5. Model verification

In this section, we provide quantitative comparison of the proposed model with a recent experimental report in literature. Recently, Minnmann *et al.*[5] used impedance spectra to obtained effective electronic and ionic conductivity values for varying solid-state cathode compositions. It

was showed that with increasing AM fraction, the effective ionic conductivity decreases, while the effective electronic conductivity increases. Non-monotonic trend in discharge capacities with increasing AM fraction is experimentally observed. We use experimental results provided in this paper to validate the modeling framework proposed in this work. Detailed list of parameters used for validation is provided in Table S5.

Table S5. Parameters used for the comparison between computational model results and experimental outcomes.

Cathode active material	NMC622
Solid electrolyte	Li_6PS_5Cl (LPSCl)
Density of NMC622	4.65 gcm^{-3}
Density of LPSCl	1.87 gcm^{-3}
CBD wt. %	0
Separator thickness	200 μm
C-rate	1
Porosity	14%
AM particle diameter	3 μm
SE particle diameter	1.5 μm
Intrinsic ionic conductivity of SE	1.6 $mScm^{-1}$
Intrinsic electronic conductivity of AM	10 $mScm^{-1}$

Figure S5 shows the comparison between modeling and experimental results depicting the final discharge capacities delivered for four different cathode compositions (AM loading of 50, 60, 70, 80 wt. %) for the discharge rate of 1C. The experimental data plotted in Figure S5 is extracted

from Figure 3 presented in Minnmann *et al.*[5], where the discharge capacities are plotted for different C-rates at varying AM loading. Quantitative trends obtained with the modeling results agrees very well with the experimental findings. As shown in Figure S5, as the AM loading is increased, discharge capacities increase, reaches maximum and then decreases. This decrease in the discharge capacities at high AM loading is attributed to the ion transport limitation in SE phase.

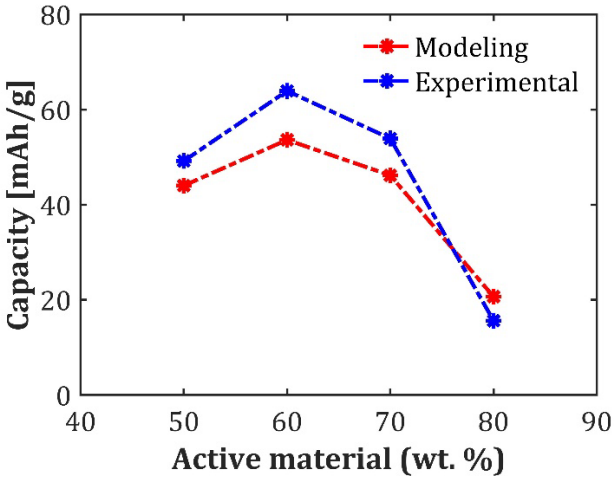

Figure S5. Comparison between modeling and experimental results showing discharge capacities for four different cathode compositions at the discharge rate of 1C. Parameters and properties taken here are tabulated in Table S3.

S6. Composition dependent active area analysis.

In this section, a deeper analysis of active area trends with varying cathode composition is performed. Figure S6(a) shows the trend of active area for varying AM loading for different CBD fractions. With the increase in CBD phase, there is significant reduction in active area, since CBD phase prevents AM-SE contact. For lower CBD fractions (0-2 wt. %), active area increases with increasing AM loading. This is because, as the AM loading increases, the available surface area of AM with which SE can come in contact increases. SE phase is also sufficiently available at lower

CBD fractions. But this is not the case with very high AM. At high CBD fraction (6 wt. %), as AM fraction is increased, there is initial increase in the active area, owing to larger AM surface area available for SE to come in contact. But further increase in the AM fraction results in slight decrease in the active area. Here, the total surface area of AM available is more, but at the same time, SE fraction is not sufficient to cover full AM surface area. Thus, there is a slight reduction in the active area. In conclusion, two main factors determining the active area are AM and SE fractions. More AM fraction leads to more availability of the surface area with which SE can come in contact. But while increasing AM fraction, SE fraction is reduced, as a result, SE phase is not sufficient to cover the full AM surface which occurs at high CBD fraction regime as can be seen from Figure S6(a). AM-AM contact also contributes towards lowering of the active area at higher AM loading. Figure S6(b) shows the variation of $\frac{\text{Active area}}{\varepsilon_{AM}}$ with the cathode composition. At all CBD fractions, the ratio $\frac{\text{Active area}}{\varepsilon_{AM}}$ first increases, reaches maximum and then decreases. This suggests that, at higher AM loading, increase in AM surface area is dominating over the increase in active area. Two main factors contribute towards this trend: (a) Insufficient SE phase cannot make contact with the whole AM surface area available, and (b) AM-AM contact further avoids the AM-SE contact in the composite cathode. Also, from Figure S6, it is worth noting that, with increasing CBD fraction, negative implications of low SE fractions on active area starts occurring at lower AM fractions.

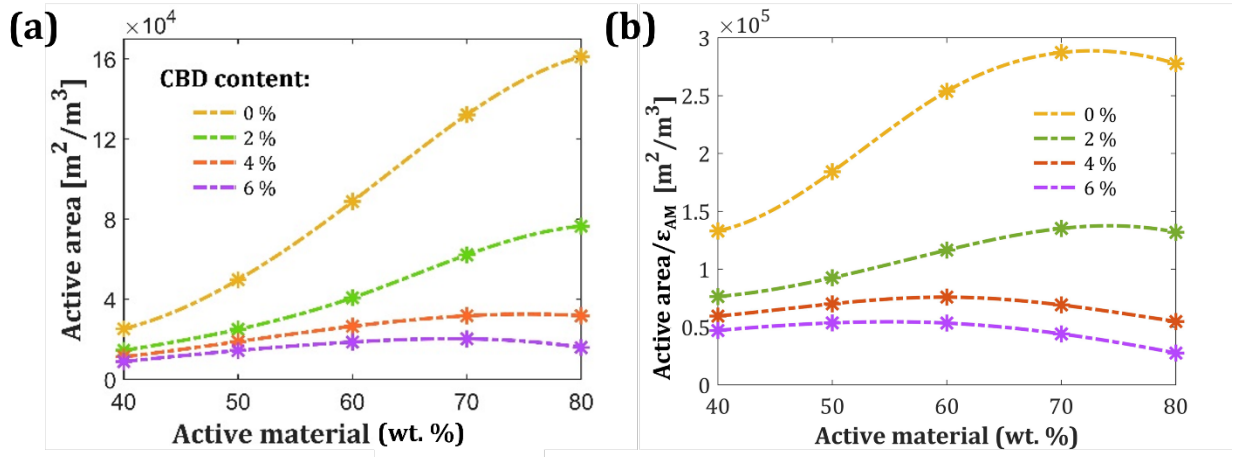

Figure S6. (a) Active area as a function of cathode composition. (b) Ratio $\frac{\text{Active area}}{\varepsilon_{AM}}$, as a function of cathode composition.

S7. Solid-solid interfaces between AM-SE particles

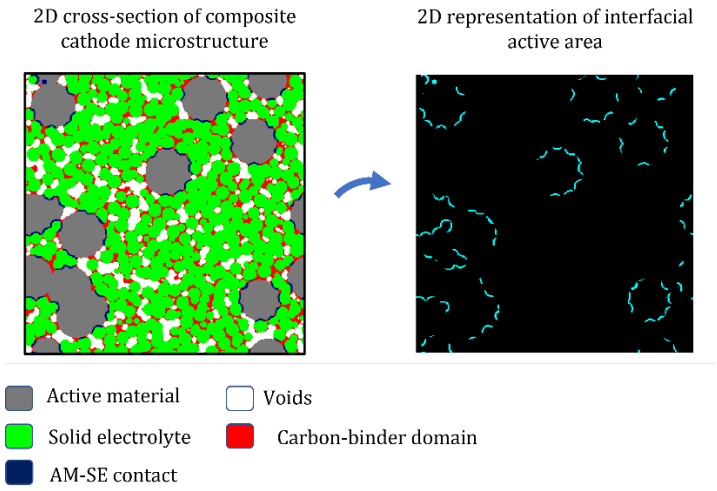

Figure S7. 2D cross-section of the composite cathode microstructure and the corresponding representation of interfacial active area for cathode composition of 40 wt. % AM, 6 wt. % CBD, 54 wt. % SE

In Figure S7, a magnified (as compared to the ones shown in Figure 2(d) and 2(e)) cross-section area of composite cathode microstructure is shown along with its corresponding interfacial active area map. In the left figure, the same interfacial active area is shown with dark navy-blue color. Unlike with liquid electrolytes, where the liquid electrolyte fully wets the AM surface, due to the solid-solid contact between the AM and SE particles, a clear reduction in the active area is seen (see Figure S7). Also, CBD phase exacerbates this scenario by preventing the AM-SE contact, as can be seen from Figure S7. At low AM content (40 wt. % in this case), active area is lower due to lower availability of the AM surface with which SE can come in contact, adding to the kinetic limitation.

References:

1. Chen, C.-F.; Verma, A.; Mukherjee, P. P., Probing the Role of Electrode Microstructure in the Lithium-Ion Battery Thermal Behavior. *Journal of The Electrochemical Society* **2017,** *164* (11), E3146.
2. Vishnugopi, B. S.; Verma, A.; Mukherjee, P. P., Fast Charging of Lithium-Ion Batteries Via Electrode Engineering. *Journal of The Electrochemical Society* **2020,** *167* (9), 090508.
3. Garcia-Mendez, R.; Smith, J. G.; Neuefeind, J. C.; Siegel, D. J.; Sakamoto, J., Correlating Macro and Atomic Structure with Elastic Properties and Ionic Transport of Glassy Li2s-P2s5 (Lps) Solid Electrolyte for Solid-State Li Metal Batteries. *Advanced Energy Materials* **2020,** *10* (19), 2000335.
4. Kremer, L. S.; Hoffmann, A.; Danner, T.; Hein, S.; Prifling, B.; Westhoff, D.; Dreer, C.; Latz, A.; Schmidt, V.; Wohlfahrt-Mehrens, M., Manufacturing Process for Improved Ultra-Thick Cathodes in High-Energy Lithium-Ion Batteries. *Energy Technology* **2020,** *8* (2), 1900167.
5. Minnmann, P.; Quillman, L.; Burkhardt, S.; Richter, F. H.; Janek, J., Editors' Choice—Quantifying the Impact of Charge Transport Bottlenecks in Composite Cathodes of All-Solid-State Batteries. *Journal of The Electrochemical Society* **2021,** *168* (4), 040537.